2013

Water Soluble Polymer Solar Cells from Electrospray Deposition

Marshall Sweet
Virginia Commonwealth University

WATER SOLUBLE POLYMER SOLAR CELLS BASED ON ELECTROSPRAY DEPOSITION

A Dissertation submitted in partial fulfillment of the requirements for the degree of Doctor of Philosophy in Mechanical Engineering at Virginia Commonwealth University.

by

MARSHALL SWEET, M.S.
Bachelor of Science, James Madison University, 2008
Master of Science, Virginia Commonwealth University, 2010

Director: James T. McLeskey, Jr., Ph. D.
Associate Professor, Mechanical Engineering

Virginia Commonwealth University
Richmond, Virginia
Spring 2013

TABLE OF CONTENTS

List of Figures iv
List of Tables vi
Nomenclature vii
Abstract viii
1. Introduction 1
    1.1 Introduction and Motivation 1
    1.2 Objectives 4
    1.3 Outline 5
2. Polymer Solar Cells 8
    2.1 History 8
    2.2 Device Concepts and Architecture 10
    2.3 Characterization 14
    2.4 Water Soluble Polymer Solar Cells 15
3. Electrospray Technology 18
    3.1 History and Introduction to Electrospray 18
    3.2 Operation 21
        3.2.1 Formation of Electrospray Jet and Droplets 25
    3.3 Application to Polymer Solar Cells 34
4. Materials 38
    4.1 PTEBS 38
    4.2 C_{60} pyrridoline tris-acid 39
    4.3 TiO_2 40
5. Characterization of PTEBS thin films from electrospray deposition 42
    5.1 Parameter Optimzation 42
        5.1.1 Effect of solvent properties 43
        5.1.2 Nozzle type and spray modes 44
        5.1.3 Flow rate 45
        5.1.4 Solution concentration 45
        5.1.5 Solvent vapor soaking 46
    5.2 Experimental 46
    5.3 Results and Discussion 47
6. Hybrid solar cells with TiO_2 nanostructures 56
    6.1 Experimental 58
    6.2 Modeling of Equivalent Circuit 59
    6.3 Results and Discussion 60
7. Polymer solar cells with water soluble active layers by electrospray deposition 67
    7.1 Experimental 70
    7.2 Results and Discussion 71
8. Conclusions 75
References 77

List of Figures

Figure 1. Solar cell efficiencies to present day. Blue trends indicate common silicon based solar cells. OPV are indicated by the red trend line in the bottom right corner [14]. 3
Figure 2. Typical polymer solar cell structures: (a) Bi-layer, (b) Bulk heterojunction [8]. 10
Figure 3. Flow of electrons in polymer solar cell [8]..... 11
Figure 4. Advanced design structures increase the interfacial surface area between the electron donor and acceptor [37]. 13
Figure 5. Folded reflective tandem polymer solar cell increases total light absorption which leads to increased photocurrents [39]..... 13
Figure 6. Typical J-V curve of a solar cell under illumination. 14
Figure 7. Electrospray deposition for thin films [57]..... 22
Figure 8. Main modes of electrospraying [57]..... 23
Figure 9. Typical electrospray capillaries: a) beveled (hypodermic), b) saw-toothed, c) blunt tipped capillary in multi-jet mode [58]. 23
Figure 10. Various configurations of electrospray systems with circular electrodes [45]. 24
Figure 11. Force balance schematic of a liquid being electrosprayed in cone-jet [57]... 25
Figure 12. Size distribution of electrosprayed droplets moving on the order of 2-3 m/s along the spray axis: (a) z=7.6 mm (b) z=25.8 mm (c) z=33.6 mm (d) z=43.6 mm. z-axis origin is at the outlet of the capillary [49]. 32
Figure 13. Evaporation and discharge of electrosprayed water droplets at 43.9°C (110°F) in nitrogen buffer gas. (Top) Variation of droplet diameter with time. The smooth line represents the predicted evaporation dynamics of a water droplet in vapor-free nitrogen gas at 43.9°C. (Bottom) Variation of droplet charge with time, represented as the number of elementary charges and as the percent of the Rayleigh limit of charge for measured droplet. Arrows indicate coulombic particle fission which occur around 90% [76]..... 33
Figure 14. Optical microscope images (x600) of the ESD P3HT:PCBM active layer onto PEDOT:PSS coated ITO/glass. A-D) show the ESD films from various mixtures of tetrachloroethane:chlorobenzene ratios of A) 90:10, B) 50:50, C) 30:70, and D) 10:90. E) Film B after thermal annealing at 160°C for 15 min. F) Film B after SVS treatment in chlorobenzene followed by thermal annealing at 160°C [77]. 35
Figure 15. (Left) AFM images of the P3HT:PCBM layers from ESD. Concentrations of acetone were (a) 5, (b) 10, (c) 15, (d) 20 volume %. (Right) J-V curves showing that the 20% acetone by volume performed the best [78]. 37
Figure 16. Chemical structure of the water soluble polythiophene PTEBS. 38
Figure 17. Absorption spectrum of a spin coated PTEBS thin film taken from a Lambda 40 UV-Vis spectrometer. 39
Figure 18. Chemical structure of C_{60} Pyrridoline tris-acid [89]. 40
Figure 19. SEM image of inner penetrating network of TiO_2 particles at 120,000x [41]. .....**Error! Bookmark not defined.**
Figure 20. Absorption spectrum for TiO_2 layer [92]. 41

Figure 21. Schematic of horizontal ESD apparatus used in experiments. 47
Figure 22. ESD spray formation from 30 G hypodermic needle [58]. 48
Figure 23. Optical microscope image at 10x of PTEBS films where a Taylor cone was (left) unstable and (right) stable. 49
Figure 24. Image of a substrate after ESD. The center circle is the cleaved mica adhered to the FTO coated glass. A 2.7 nm layer of platinum was sputtered onto the mica and glass. The top left and bottom right corners are free of PTEBS as they were conductively taped to the grounded aluminum plate of the electrospray apparatus. 49
Figure 25. AFM topology of mica substrate covered with PTEBS particles after 1.5 minutes of ESD. 50
Figure 26. AFM profile image of PTEBS after 1.5 minutes of ESD. 51
Figure 27. Particle diameter histogram of 25 μm^2 after ESD for 3 minutes. 51
Figure 28. AFM topology of mica substrate covered with PTEBS particles after 5 minutes of ESD. 52
Figure 29. AFM profile image of PTEBS after 5 minutes of ESD. 53
Figure 30. AFM topology of mica substrate covered with PTEBS thin film after 40 minutes of ESD. 54
Figure 31. AFM angled image of PTEBS thin film after 40 minutes of ESD. 54
Figure 32. Absorption spectrum of PTEBS thin films from ESD (600 nm and 1.2 μm) and from drop casting (7 μm). 55
Figure 33. Energy band diagram for FTO/TiO2/PTEBS/Au devices. The band gap of PTEBS is ~2 eV. The estimated range of the LUMO is 2.7~-3.2 eV and the HOMO ranges from and -4.7~-5.2 eV [40]. The work functions of FTO, TiO_2, and gold are -4.4 eV [122], -4.2 eV [118], and -5 eV [123], respectively. 57
Figure 34. Schematic of bilayer heterojunction hybrid solar cell with configuration of glass/FTO/TiO_2/PTEBS/Au [40]. 58
Figure 35. Equivalent circuit of a solar cell. 59
Figure 36. Average $J - V$ curves of 15 different devices from each deposition method of the PTEBS layer. The error bars show the standard deviation of the current along each measured voltage value. Error bars were omitted from points at the intersection for clarity. 61
Figure 37. SEM image of the inter-penetrating nanocrystalline TiO_2 film at 120,000x magnification. 62
Figure 38. AFM image of PTEBS film from ESD. 63
Figure 39. Illuminated average $J - V$ curves from experimental data and computational models. Model lines varying J_{ph} held a constant $J_0 = 2.2 \times 10^{-7}$ mA/cm^2. Model lines varying J_o held a constant $J_{ph} = 0.047$ mA/cm^2 65
Figure 40. Dark $J - V$ curves of experimental data and model. 66
Figure 41. Energy band diagram of PSC with bulk heterojunction active layer comprised of water soluble materials, PTEBS and C_{60} derivative. 69
Figure 42. J-V Curves of PSC with Water-Soluble Active Layers from ESD. The ratio of the polymer PTEBS to C_{60} tris-acid is varied from 1:1 to 1:3. 72
Figure 43. SEM image of aluminum electrode above an active layer from ESD. 73
Figure 44. Illustration of active layers with varying PTEBS:C_{60} ratios. Percolation threshold of C_{60} was achieved in devices B and C, where C_{60} molecular chains extend randomly throughout the active layer. 74

List of Tables

Table 1. Constants for variables in equation 3.12 to determine mean droplet size. 28
Table 1.Table of minimum, maximum, and average values of short circuit current (J_{sc}), open circuit voltage (V_{oc}), and efficiency (η) of 15 different HSC with electron donor layers from ESD and spin coating. 61

Nomenclature

A	area of capillary
C_c	Cunningham slip correction factor
c_d	mass concentration of cloud
d	Droplet size
d_c	capillary diameter
d_o	droplet diameter with no applied voltage
E	electrodynamic force
E_{ds}	Electric field on surface of a single charged droplet
g	gravity
L_g	gravitational force volume density
L_ρ	inertial force volume density
Q	liquid volumetric flow rate
q	charge
Q_d	magnitude of electric field on a charged droplet
r	radius of droplet
t	time
V	voltage
V	volume
α	constant of spray conditions
γ_l	liquid conductivity
ε_o	electric permittivity of free space
ε_r	dielectric constant of liquid
η_g	gas dynamic viscosity
Λ	tensor of electromagnetic and polarization stresses on the inter-phase surface
Ξ	tensor of surface tension
Π	stress tensor acting on liquid surface
ρ_l	density of liquid
ρ_q	volume charge density
σ_l	surface tension of liquid
τ_{exp}	time constant of cloud expansion
Φ_d	drag force volume density
I_{sc}	short circuit current density
V_{oc}	open circuit voltage
R_{sh}	shunt resistance
R_s	series resistance
I_0	saturation current
I_{ph}	photo generated current
η	diode ideality factor

Abstract

WATER SOLUBLE POLYMER SOLAR CELLS BASED ON ELECTROSPRAY DEPOSITION

A Dissertation submitted in partial fulfillment of the requirements for the degree of Doctor of Philosophy in Mechanical Engineering at Virginia Commonwealth University.

by
MARSHALL SWEET, M.S.

Virginia Commonwealth University, 2013

Director: James T. McLeskey, Jr., Ph. D.
Associate Professor, Mechanical Engineering

This dissertation reports the fabrication and characterization of thin films from the water soluble polymer sodium poly[2-(3-thienyl)-ethyloxy-4-butylsulfonate] (PTEBS) by electrospray deposition (ESD). Contiguous thin films were created by adjusting the parameters of the electrospray apparatus and solution properties to maintain a steady Taylor cone for uniform nanoparticle aerosolization and controlling the particle water content to enable coalescence with previously deposited particles. The majority of deposited particles had diameters less than 52 nm. A thin film of 64.7 nm with a root mean square surface roughness of 20.2 nm was achieved after 40 minutes of ESD.

Hybrid Solar Cells (HSCs) with PTEBS thin films from spin coating and electrospray deposition (ESD) were fabricated, tested, and modeled. A single device structure of FTO/TiO_2/PTEBS/Au was used to study the effects of ESD of the PTEBS layer on device performance. ESD was found to double the short circuit current density (J_{sc}) by a factor of 2 while decreasing the open circuit voltage (V_{oc}) by half compared to spin coated PTEBS films. Comparable efficiencies of 0.009% were achieved from both device construction types. Current-Voltage curves were modeled using the characteristic solar cell equation showed a similar increase in generated photocurrent with a decrease of

two orders of magnitude in the saturation current in devices from ESD films. Increases in J_{sc} are attributed to increased interfacial contact area between the TiO_2 and PTEBS layers, while decreases in V_{oc} are from poor film quality from ESD.

Polymer solar cells (PSCs) with water-soluble active layers deposited by ESD were fabricated and tested. The water soluble, bulk heterojunction active layers consisted of PTEBS and the fullerene C_{60} pyrrolidine tris-acid. A single device structure of ITO/PEDOT:PSS/bulk(PTEBS+C_{60})/Al was used to study the effect of PTEBS to C_{60} tris-acid ratio on photovoltaic performance. An active layer ratio of PTEBS:C_{60} tris-acid (1:2) achieved the highest power conversion efficiency (0.0022%), fill factor (0.25), and open circuit voltage (0.56 V). The percolation threshold of C_{60} was achieved between 1 part PTEBS and 2 to 3 parts C_{60}. Increasing the C_{60} tris-acid ratio (1:3) improved short circuit current, but reduced the open circuit voltage enough to lower efficiency.

1. INTRODUCTION

1.1 Introduction and Motivation

The International Energy Agency has reported that in the year of 2010, 80% of the world's electricity was from non-renewable sources (67.1% from the combustion of fossil fuels and 12.9% from nuclear energy) [1]. Each of these non-renewable sources negatively impacts the environment in ways such as acid rain, radioactive waste, mining destruction, and the generation of greenhouse gases. Not only do these non-renewable sources inflict harm upon the environment, but they are also limited in supply. Petroleum oil makes up 34.4% of the total energy supply, mainly in the production of gasoline, so it has been the most studied energy source for predicting the longevity of its existence. In 1956, M. King Hubbert predicted the peak of oil production to occur between 1965 and 1970 [2]. Since Hubbert's prediction, many other models have been developed every few years delaying the year of peak oil production based on improved mining technology. However, all predictions agree that there will be a peak in production, followed by a period of decline, and this goes for all non-renewable sources. It is imperative that alternative clean energy sources be investigated.

The sun is a 1.39×10^6 km sphere of gaseous matter with an average surface temperature of 5762 K and sends between 1300 – 1400 W/m^2 (at ground level this number decreases to 1000 – 1120 W/m^2) of energy to the Earth's atmosphere [3]. Not only does the sun provide the Earth with an abundance of energy, the sun is also expected to "rise" every day for a very long time (also known as renewable energy). The U.S. Department of Energy has suggested that covering 0.16% of the Earth's surface with 10% efficient solar cells would provide approximately 2×10^{13} W of electricity, which is more

than the current energy demand of the whole planet [4]. The need to research and develop inexpensive methods of harvesting the sunlight for conversion to electricity is the stimulating force of scientific research for efficient, low cost solar cell devices. Polymer solar cells (PSCs) have emerged as the front runner because of their potential for cheap and easy fabrication of devices [5].

Polymer Solar Cells have gained considerable attention in recent years due to their low cost, ease of fabrication, thin film applications, and material safety. PSCs generally refers to solar cells that consist of an organic polymer electron donor and a fullerene (C_{60}) or an inorganic material (TiO_2, ZnO, CdSe, etc.) as the electron acceptor. PSC efficiencies are low (maximum 11.1%) compared to the efficiencies of common silicon based photovoltaics, 16 to 25% [6,7]. Nonetheless, the high cost of materials and energy required to make silicon solar cells are making PSCs a popular area of interest. PSC fabrication is often done by printing or coating at room temperature from solution. Thermal evaporation of materials for PSCs is also done at considerably lower temperatures than the high temperature processing steps required by silicon photovoltaics (exceeding 1000°C) [8].

Efficiencies of PSC devices are expected to continue to increase whereas the efficiencies of silicon devices have approached their theoretical limits over the last 20 years. Figure 1 shows the efficiency trends of different types of photovoltaic devices since 1976. The blue lines indicate silicon based solar cells, which are nearly straight lines, indicating minimal improvement upon efficiency. The maximum silicon PV efficiencies to date is 27.6% which is close to the Shockley and Queisser maximum theoretical efficiency limit of p-n junction silicon solar cells of 30% [9]. The red line in

the bottom right corner of Figure 1 shows the increasing trend line of OPV efficiencies. The highest PSC efficiencies to date are between 8.3 and 9.2% [7], which is nearly double the maximum efficiency obtained in 2005 [6]. The current research goal for PSC device efficiency is to exceed 10% because this is where their low cost offsets their lower efficiencies and lifetimes (5-10 years) to make them a more economical choice over common silicon PV devices. Currently, the cost to fabricate and install silicon solar cells is $2-3/Watt for silicon solar cells and $1.00-2.83/Watt for PSCs [10,11]. Currently the cost of electricity in the US is about $0.07 – 0.13/kWh [12]. The levelized cost of electricity (LEC) for a silicon solar cell is between $0.25 – 0.65/kWh [13]. Assuming a PSC with 5% efficiency and a 5 year lifetime would have a LEC between $0.49 - $0.85/kWh. In order to achieve a LEC of $0.07/kWh, PSCs would need to have 15% efficiency and a lifetime between 15 – 20 years [11].

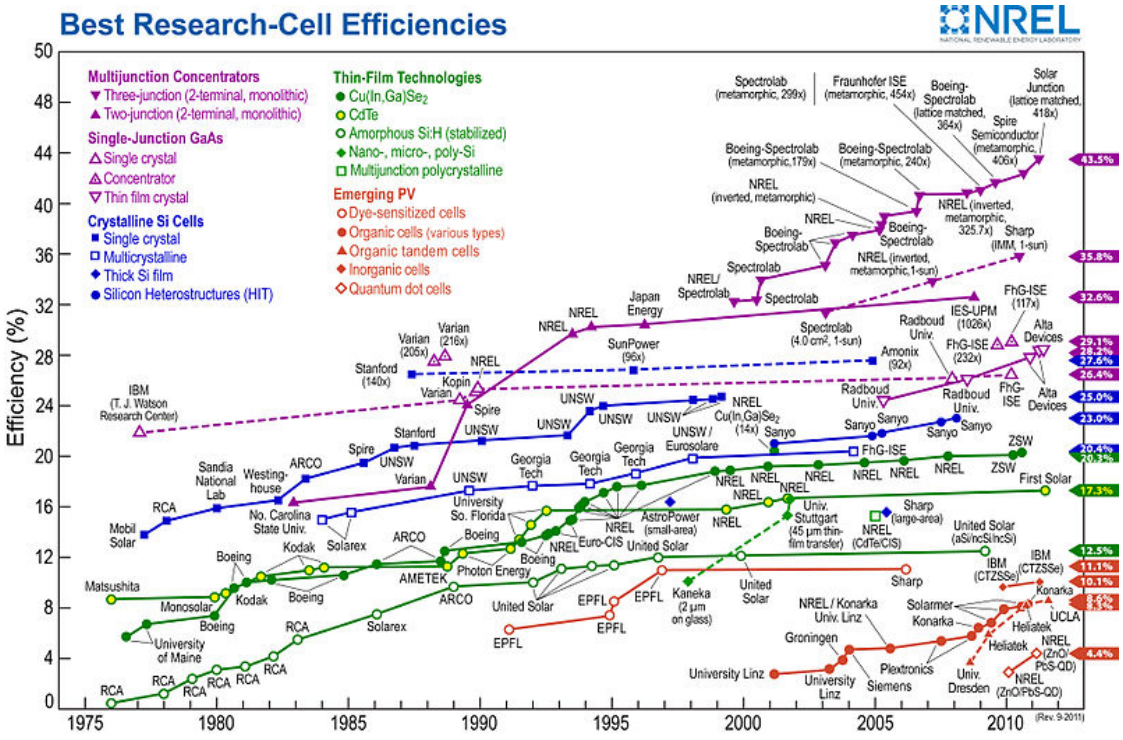

Figure 1. Solar cell efficiencies to present day. Blue trends indicate common silicon based solar cells. OPV are indicated by the red trend line in the bottom right corner [14].

1.2 Objectives

The efficiency of PSCs is intimately linked to the processing conditions during device fabrication, and commercialization of PSCs will ultimately depend on successful large scale fabrication. Traditional laboratory PSC devices are commonly prepared by a two step solution process where two different layers are spin cast. The first layer being a dispersion of PEDOT:PSS in water, and the second being a bulk heterojunction active layer dissolved in an organic solvent. However, spin casting is a low throughput and high waste process since much of the polymer is lost due to the non-recyclable polymer displaced from the high rotational speeds. A second problem with the traditional laboratory fabrication method is the inability for consecutive layering from common solvents. In order to add multiple layers of polymer, another solvent orthogonal to the previous layer would be needed. This hinders simple/cheap solution based processes in favor of expensive evaporation deposition methods.

Electrospray deposition (ESD) is a method of depositing thin films which can overcome the problems associated with spin coating. Firstly, ESD is favorable to commercialization since it is cheap, efficient (minimal waste), and has a high throughput. Secondly, it overcomes the solubility issue between two adjacent layers. ESD generates atomized particles which are nearly dry upon deposition so that it doesn't affect the previous layer.

Another major issue facing the commercialization of PSCs is the sensitivity of the polymers to atmospheric conditions. Popular conjugated semiconducting polymers used in traditional laboratory fabrication are soluble in organic solvents and are known for oxygen degradation which adversely effects PSC lifetimes [15]. Traditional laboratory

fabrication is often carried out in inert nitrogen filled glove boxes. Once the final electrode is deposited, the PSCs can be sealed. By using water soluble polymers, oxygen sensitivity is assumed to be avoided since water contains oxygen. Being able to work in atmospheric conditions would significantly reduce ease and cost of commercializing PSCs. PSC devices fabricated through water soluble approaches are also more favorable since organic solvent exposure include toxicity to the nervous system, reproductive damage, liver and kidney damage, respiratory impairment, cancer, and dermatitis [16].

The objective of this work is to investigate the application of ESD of water soluble polymer (specifically PTEBS) thin films in the fabrication of PSCs. Using a water soluble polymer enables us to stay true to the mission of producing environmentally friendly alternative energy. Water solubility combined with ESD enables fabrication of PSCs under atmospheric conditions with high throughput, which is more favorable to commercialization. ESD will enable deposition of two consecutive water soluble layers such as PEDOT:PSS and a bulk heterojunction layer of the water soluble polymer and a water soluble fullerene derivative. Fabrication of hybrid solar cells with inorganic electron acceptors (ZnO nanorods and TiO_2 inner penetrating nanostructure) will also be investigated to compare device performances from traditional spin casting methods to ESD. The different geometries of the inorganic semiconductors will provide insight to the limits of the ESD method for creating thin films on different surfaces.

1.3 Outline

Chapter 2 presents a background and literature review of PSCs. A brief history is presented before device concepts/operation and architecture are explained. Basic

characterization methods of solar cells are then discussed. A brief history of water soluble polymer solar cells focusing on the PTEBS is also presented.

Chapter 3 is dedicated to the electrospray technology. A brief history and introduction to electrospray is presented, followed by a detailed discussion of ESD operation and formation of electrospray jet and droplets. ESD and its application to PSCs, including the two previously reported instances of PSCs from ESD, will be presented at the end of the chapter.

Chapter 4 gives a brief overview of the chief materials used in the PSCs' active layers fabricated in this work. The only polymer electron donor used was the water soluble polymer PTEBS. The organic electron acceptor, water soluble C_{60} pyrridoline tris-acid, was used in combination with PTEBS to create bulk heterojunction polymer solar cells (PSCs) with a fully water soluble active layer. Inter-penetrating layers of TiO_2 were used as the electron acceptor in the fabrication of hybrid solar cells (HSCs).

Chapter 5 is dedicated to the characterization of PTEBS thin films from electrospray deposition (ESD). The multiple parameters involved and their effect on the ESD of PTEBS thin films are analyzed for suitable film morphology. Substrates are analyzed by atomic force microscopy (AFM) after different durations of ESD to understand the film formation process.

Chapter 6 focuses on the comparison of TiO_2 Hybrid Solar Cell (HSC) devices with electrostatically sprayed PTEBS layers versus devices with traditional spin coated PTEBS films. The characteristic solar cell equation is then modeled to gain insight to the variations of device parameters between the two device constructions.

Chapter 7 discusses the fabrication of PSCs with fully water soluble active layers by ESD. The ratio of C_{60} pyrridoline tris-acid to PTEBS is optimized for maximum efficiency.

Chapter 8 is a summary of conclusions from the results discussed in the preceding chapters.

2. POLYMER SOLAR CELLS

Polymer Solar Cell (PSC) devices are diodes that generate a photocurrent when light is incident upon their active layer. The active layer consists two sub-layers: a conjugated polymer layer(s) and a second layer of organic and/or inorganic material. The conjugated polymer (electron donor) is responsible for absorbing light and donating an electron to the organic/inorganic material (electron acceptor), which then transfers electrons to the anode. The polymer donors are typically polythiophenes or poly(p-phenylene vinylene) derivatives that behave like semiconductors but are of a plastic material. The polymer molecular structures have overlapping pi-bonds allowing electrons and holes to move between energy levels upon excitation. Photoelectric manipulation of electrons and holes in these uniquely structured polymers is the basis of PSCs [17]. The electron acceptor layer is often comprised of nanoparticles or other polymers. Common organic electron acceptor materials include carbon nanotubes, Buckminster fullerenes, phthalocyanine, perylene, and their derivatives [5]. Common inorganic acceptors include TiO_2, ZnO, Si, CdSe, PbSe, and PbS [18]. PSCs that contain inorganic acceptors are also known as hybrid solar cells.

2.1 History

The first silicon solar cell was fabricated in 1954 by Bell Labs from crystalline silicon with an efficiency of 6% [19]. Commercially available crystalline silicon solar cell efficiency has since in been improved to 25% [20], and currently account for 95% of the total solar cell market [21]. Amorphous silicon solar cells were invented in 1974 at RCA Laboratories as a thin alternative to crystalline silicon [22]. Amorphous silicon solar cells are made by evaporating silicon to produce amorphous thin films requiring less

material and a lower cost of production [23]. Amorphous silicon solar cells have lower efficiencies than crystalline (less than 15%) due to high defect densities from evaporation processing [24]. However, the thin film approach used in amorphous silicon fabrication has allowed further development of solar cells from silicon and a variety of other materials such as gallium arsenide, cadmium telluride, dyes, and polymers [14].

Polymer solar cells consisting of an organic semiconductor layer sandwiched between two metals were first reported in the late 1960s and early 1970s [25]. The organic semiconductor initially used by Ghosh et al. was tetracene. In 1977, Shirakawa et al. introduced doped polyacetylene as a new class of conducting polymers in which the electrical conductivity can be systematically and continuously varied over a range of eleven orders of magnitude [26]. Since then, electronic devices such as organic light emitting diodes (OLEDS) and polymer solar cells have been the focus of extensive research.

A breakthrough in PSC research occurred in the mid 1980s with the introduction of a two component active layer [27,28]. Polymer solar cells we fabricated with two materials working in alliance: a light absorbing polymer donating electrons to an organic or inorganic electron acceptor. This was the first time PSC efficiencies surpassed 1%. In 1992, a second major breakthrough occurred when Sariciftci et al. created a PSC using the polymer MEH-PPV and buckminsterfullerene (C_{60}) as the electron acceptor [29]. The introduction of the two part active layer and the use of C_{60} as the electron acceptor have been the most influential factors in PSC research to date. P3HT has widely been considered the best commercially available conjugated polymer for PSCs since they

produce the highest average efficiency (5%) of all devices reported in the year of 2010 [30].

2.2 Device Concepts and Architecture

The most common PSC device structures currently being researched are the bi-layer and the bulk heterojunction (BHJ) structures as shown in Figure 2. Both structures are typically built on top of a glass substrate covered with a transparent conducting oxide (TCO) that acts as the anode. Indium or fluorine doped tin oxide are the most common TCO's. On top of the TCO is a hole-conducting polymer layer of (PEDOT:PSS) that prevents short circuits. The next layer is the active layer where light absorption and the photocurrent generation occur. On top of the active layer is a metal cathode (Al, Au, Ni, etc.). A bi-layer structured device has two distinct layers where the active layer is comprised of an electron donor and an electron acceptor layer. In a BHJ structure, the active layer is a blend of the both the electron donor and acceptor [8].

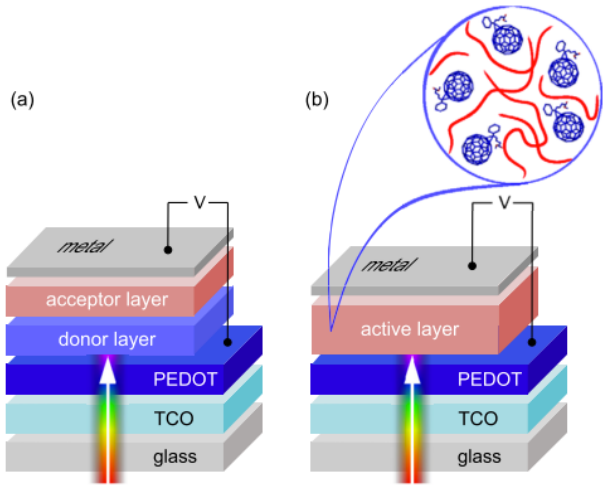

Figure 2. Typical polymer solar cell structures: (a) Bi-layer, (b) Bulk heterojunction [8].

The PSC devices generate a photocurrent due to the engineered structure of the polymer layers' energy band-gaps and the electrodes' work functions. Light passes through the TCO and PEDOT layer and is absorbed in the active layer by the

semiconducting polymer electron donor as seen in Figure 3. The absorption range is generally fairly narrow, between 450-600 nm (2.0-1.9 eV), and differs amongst individual polymers. The electron donor absorbs light in a narrow wavelength region which varies depending on the polymer's band gap. The band gap is determined by the energy difference between the highest occupied molecular orbit (HOMO) and the lowest unoccupied molecular orbit (LUMO) of electrons. The polymer's HOMO and LUMO levels are caused by the ability of electrons to jump from overlapping pi-bond clouds in the polymer chains [17].

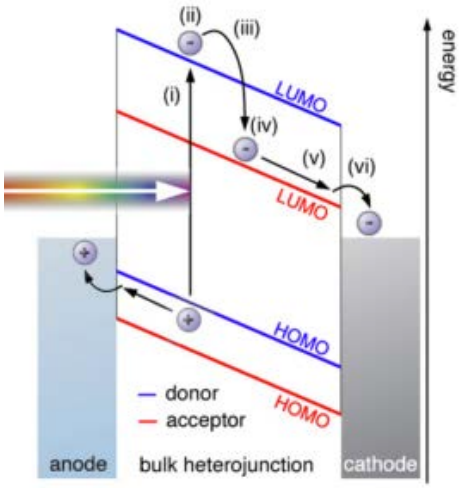

Figure 3. Flow of electrons in polymer solar cell [8].

The donor absorbs light and an electron-hole pair, or exciton, is generated. When the exciton reaches an interface between the polymer donor and the electron acceptor, the electron is excited to the LUMO and the hole maintains the displaced electron's position in the polymer's band gap. The excited electrons diffuse to the acceptor interface and lose energy when they fall into the electron acceptor's LUMO level. The electron is then transported from the acceptor's LUMO level to the cathode. The cathode's work function needs to be less than the donor's LUMO but greater than the donor's HOMO. Once the

electron goes to the cathode, the hole on the donor's HOMO travels to the anode and completes the electrical circuit.

The exciton generated after absorption by the polymer has a very limited diffusion range, 3-10 nm in typical polymer donors, to meet a donor/acceptor interface before it loses energy and the electron returns to the polymer donor's HOMO [31]. The minimum film thickness for effective optical absorption of sunlight is 50-250 nm. Efficient solar cells require excitons to be generated within a nano scale interpenetrating bi-continuous network of electron donor and acceptor materials through the active layer [32].

P3HT with a thickness of 240 nm is still only able to absorb 21 % of the sun's incident photons. Active layer thicknesses above 150 nm result in high recombination rates due to the polymer's low carrier mobility [33]. Another major obstacle these conjugated polymers present to PSC is that their band gap is too large and the absorption bandwidth of these materials is too narrow to absorb a large fraction of useful energy of the solar spectrum. Developing new polymers with lower band gaps and wider absorption ranges is an increasing area of research in OPV [34].

Hybrid PSCs consist of a polymer electron donor and an inorganic semiconductor which assumes the electron acceptor role. Hybrid PSCs take advantage of inorganic semiconductor's high electron mobility [35,36]. Engineering the interface structure between the electron donor and acceptor can also improve hybrid PSC cell performance by lowering recombination rates and electron flight distances. Inorganic nanoparticles and/or nanostructures are used as the electron acceptor in hybrid solar cells. These nanoparticles (TiO_2 NR or nanoribbons) and nanostructures (ZnO nanorods) increase the interfacial surface area as shown by Lin et al. in Figure 4.

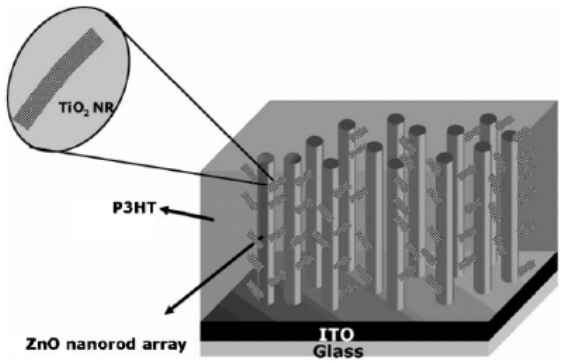

Figure 4. Advanced design structures increase the interfacial surface area between the electron donor and acceptor [37].

Other advanced design structures for increasing the interfacial surface area via nanolithography are also being researched. Electron donor/acceptor layers are being nano-imprinted so that the polymer layers mimic the design of nanorods. However, nano-imprinting and lithography methods have less resolution than self assembled methods which are more difficult to control [38]. Another advanced design is to include two OPV devices connected in parallel. Each device has a different polymer with differing absorption spectra that complement each other (Figure 5). By angling the two devices with a reflective back electrode, a wider spectrum of light can be absorbed [39].

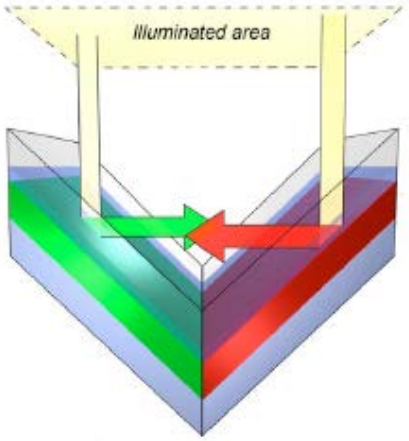

Figure 5. Folded reflective tandem polymer solar cell increases total light absorption which leads to increased photocurrents [39].

2.3 Characterization

The primary characteristic of a solar cell is the efficiency (η). The efficiency is a measure of how well a device performs based on the ratio of electrical power output divided by the power of incident light. The power output of a solar cell is measured and characterized by analyzing the relationship between its current density and voltage known as the J-V curve. The J-V curve will appear as a diode if measured in the dark, and will shift into the 4th quadrant, as show in Figure 6, when measured in the light since a photocurrent will be generated.

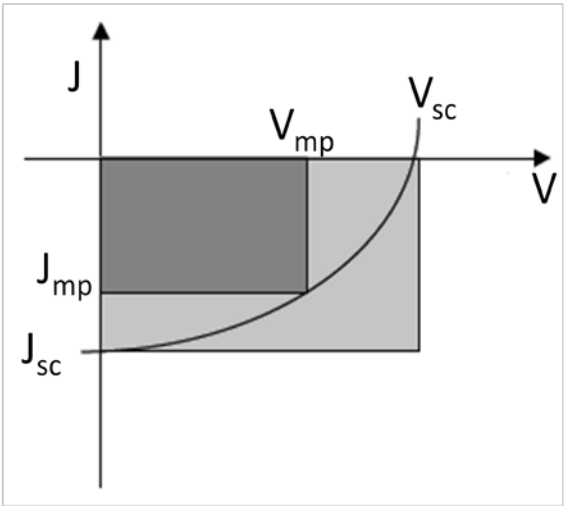

Figure 6. Typical J-V curve of a solar cell under illumination.

The J-V curve of a solar cell crosses the current axis (y-axis) under short circuit conditions (J_{sc}), and crosses the voltage axis (x-axis) under open circuit conditions (V_{oc}). The dark shaded region inside of the J-V curve in Figure 6 depicts the largest square that can be formed inside of the curve. The asymptotes signify the current and voltage conditions where the maximum power is obtained. The maximum power, open circuit voltage, and short circuit current are all interrelated parameters that are used to compute the power output, efficiency, and other characteristics of a solar cell.

The open circuit voltage (V_{oc}) is the built-in electrical potential between the two electrodes of a solar cell when there is no external load and light is present. V_{oc} is the maximum voltage sustained by the device, and is measured when the load is connected to infinite resistance. The built in electrical potential also causes a drift in the photogenerated charges of the device known as the short circuit current (J_{sc}). J_{sc} is the measure of the maximum current sustained by the device, and is measured when the load has zero resistance.

The ratio between the maximum electrical power, and the theoretical maximum of electrical power estimated from the product of the J_{sc} and V_{oc} is called the fill factor (FF):

$$FF = \frac{P_{max}}{P_{theoretical}} = \frac{J_{mp}V_{mp}}{J_{sc}V_{oc}}$$

The J_{mp} and V_{mp} are the current density and voltage of where maximum electrical power output is obtained. Fill factor is a measure of quality of the device, and it can also be viewed as the ratio between the dark and light shaded boxes in Figure 6. Devices with higher fill factors are able to extract more electrical power from a more constant current over a higher voltage.

Solar cell efficiency is a measure of how effectively a device converts sunlight into electrical energy by comparing the total power input from the sun to the total power output from the device. The efficiency (η) is given by the following equation:

$$\eta = \frac{J_{mp}V_{mp}}{P_{light}} = \frac{FFJ_{sc}V_{oc}}{P_{light}}$$

2.4 Water Soluble Polymer Solar Cells

Recently, more and more attention has been paid to the fabrication of PSC through aqueous approaches considering the green chemistry concept. Typical laboratory

solution processing uses organic solvents (chloroform, chlorobenzene, toluene, xylene, hexane, etc.) to dissolve the conjugated polymer. Water is a more favorable solvent since exposure to organic solvents can result in toxicity to the nervous system, reproductive damage, liver and kidney damage, respiratory impairment, cancer, and dermatitis [16]. Water soluble polymers are also less susceptible to oxygen degradation which adversely affects PSC lifetimes since water contains oxygen [15].

The first water soluble PSC was reported in 2005 by Qiao and McLeskey using the water soluble polythiophene PTEBS. The bilayer PSC device structure of FTO/TiO_2/PTEBS/Au had an efficiency of 0.13% [40]. Subsequently, they improved device efficiency to 0.17% by adding a TiO_2 buffer layer (FTO/TiO_2/(TiO_2+PTEBS)/Au). The buffer layer improved the interfacial contact which increased the shunt resistance [41].

The highest PSC device from the water soluble polymer PTEBS reported is 0.43% by Yang, Garcia, and Nguyen. The bilayer device structure they used was ITO/PTEBS/C_{60}/BCP/Al where the C_{60} was the electron acceptor and the BCP functioned as an exciton blocking layer. Their device used thermal evaporation to deposit the layer of C_{60}, however it is the highest efficiency achieved using PTEBS [42].

The highest efficiency of any PSC device fabricated from a water soluble polymer was 2.14% by Yang et al. A water soluble poly(phenylene vinylene) (PPV) was as the polymer electron donor and cadmium telluride (CdTe) was the electron acceptor as well as zinc oxide (ZnO). The device configuration was ITO/PEDOT:PSS/(PPV+CdTe)/ZnO/Al. However, the fabrication methods used didn't stay true to the clean chemistry approach since organic solvents were used to fabricate the

cadmium telluride nanocrystals. Fabrication was also carried out in nitrogen and not in open air. The high efficiency is linked to the large absorption spectrum of the CdTe [43].

A PSC has also been fabricated from exclusively using aqueous approaches by Sondergaard et al. They synthesized their own polymer by creating poly-3-carboxydithiophene (P3CT) and then decarboxylating it at high temperatures to form a basic polythiophene. They also created monodisperse clusters of C_{60} from PCBM in water through forced precipitation by addition of a THF solution in water. While neither part of the active layer was water soluble, they were both capable of being suspended in water and deposited into thin films via spin casting. A water based silver paste was then screen printed for the top electrode. Device efficiencies were only 0.7%, but this was a critical first step towards creating PSCs in an environmentally friendly method with water as the only processing solvent [44].

3. ELECROSPRAY TECHNOLOGY

The term electrospray, or electrospraying, is used when electrical forces are used for liquid nebulization. A high electrical potential is applied to a liquid supplied through a metallic capillary tube to disperse a liquid into fine droplets. The liquid at the tip of the capillary forms a Taylor cone, through which the liquid breaks apart into droplets at the apex. The droplets formed are highly charged to approximately half of the Rayleigh limit and continue to repel from each other until deposition due to their like charges. The droplets may be on the order of 10's of nanometers and can ideally be controlled to an extent by controlling the electric potential. This chapter will focus on the use of electrospray deposition to create uniform thin films, with a particular focus on its application to solar cell fabrication [45].

3.1 History and Introduction to Electrospray

During the late 16th century William Gilbert was the first to observe and report that a drop of water deformed into a cone when in the presence of a charged piece of amber. He did not document any observations related to liquid nebulization and likely did not know cone deformity was related to electrospraying [46].

The first widely known observation of liquid being electrosprayed was in the 18th century by Abbe Nollet. Nollet was researching the art of healing via electricity. He constructed a high voltage generator and connected human subjects to it for 15-45 minutes. He discovered that a person who was highly electrified would not bleed normally if he were to cut himself. Instead of blood dripping from the wound, it would spray. He then connected vessels of blood to the system and achieved the same spraying phenomenon [47]. It is unknown if he experimented with any other liquids.

In 1882 Lord Rayleigh published the first theoretical work on electrospray nebulization. He stated that the magnitude of charge on a droplet that produces an electrostatic force greater than the surface tension force of the liquid, would lead to the formation of a jet and eventually droplet nebulization. This charge is known as the Rayleigh limit, which was experimentally proven over 100 years later [48,49].

Sir Geoffrey Taylor wrote the first blueprint for an electrospraying device in 1964. Taylor was able to show that a drop of water became elongated when in the presence of an electric field, and that tiny jets of water extended from the droplets. As the electric field increased beyond a critical electric field the elongated drop becomes unstable. Through experiments he noticed that when the length of the drop is 1.9 times its equatorial diameter, it lost stability. He was able to calculate the critical electric field based on Rayleigh's principle of balancing electrical and viscous forces. He then built an apparatus in his lab to show that his calculations agreed with experimental data to within 1% [50]. The elongated drops formed under the presence of an electric field are now formally known as Taylor Cones.

John Fenn led the technology into the modern era by developing Electrospray Mass Spectrometry (ESMS). ESMS is a widely used technique across many disciplines of research namely medicine and biology. Its principles rely on electrospraying a fluid into molecules and being able to identify the molecules of said fluid by measuring them with mass spectrometry [51]. This application was a tremendous breakthrough in the biomedical fields and renewed interest into electrospray technology.

Research in electrospray technology increased during the late 20th century after further developments improved typically low throughputs. Low throughput was the

major limiting factor in its widespread use in industry which is overcome by multi-nozzle systems [52,53], linear-slit nozzle systems [54], mechanical spraying by rotary [55], and pneumatic atomizers with grounded capillary and a high voltage induction electrode [45,56].

Adjusting the liquid flow rate and the electric voltage can largely control the size and charge of atomized droplets. Controlling external field(s) can also control the motion of the atomized droplets to focus/disperse. Deposition of a charged spray or solid particles onto grounded, or oppositely charged, surfaces can be more efficient than deposition of uncharged particles. Consequently, this makes electrospray nebulization an ideal deposition method for uniform thin films (less than 100 um). Apparatuses for supplying high electrical potential (1kV – 30kV) and pumps are relatively simple and cheap [45]. Electrospray technology can be used to create thin films from coating-material solution or colloidal suspensions. The droplets can also undergo chemical reactions during their flight to the substrate. Morphology of the thin film can be affected by a number of parameters such as deposition rate, temperature, humidity or anything that affects the solvent evaporation rate during droplet flight to deposition.

Electrospray nebulization has several advantages over conventional mechanical atomizers:

1. Droplet size is small (can be in the nanometer range)
2. Standard deviation of droplet size is typically small and contributes to more uniform layers
3. Charged droplets are self-dispersing due to their electrical repulsion and this minimizes coagulation

4. The flow of charged droplets can be focused/dispersed using electric field gradients
5. Deposition efficiency of a charged spray is orders of magnitude higher than for un-charged droplets, leading to lower fabrication costs

There are a wide variety of applications that involve the spraying of liquids, but the question remains the same, "Why may it be advantageous to charge the spray drops?" The answer is almost always the same: to distribute the liquid in a controlled and predetermined way. By introducing charged droplets and/or an electric field to the spray zone, trajectories of the drops and the deposition structure can be controlled in ways that are not possible without applied electrostatic forces.

3.2 Operation

A typical electrospray deposition set up (Figure 7)has three essential components: a fluid source pump, a high voltage supply, and a metal deposition plate. The fluid source pump is typically a syringe pump holding a syringe with a metal needle. The volumetric flow rate is typically in the range of 0.1 to 10 ml/h [45]. The metal needle is typically connected to the high voltage supply (theoretically the needle can be positive or negative biased, or grounded, as long as an electric field exists between the needle and the deposition plate) and the deposition plate is grounded. Voltages are typically greater than 1kV but rarely exceed 20 kV. When the voltage is too high, the air begins to conduct current between the capillary and the ground plate, and oxygen in the air is broke down to form ozone.

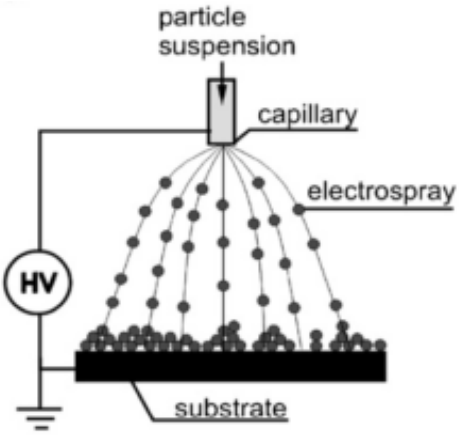

Figure 7. Electrospray deposition for thin films [57].

The electrical charge needed to overcome the surface tension forces in a droplet is known as the Rayleigh Limit given by the following equation:

$$q = 2\pi(16\sigma_l\varepsilon_0 r^3)^{1/2} \qquad (3.1)$$

where σ_l is the liquid surface tension, ε_0 is the electric permittivity of the free space, and r is the droplet radius [48]. As the electrical charge is increased beyond the Rayleigh Limit, the mode of spraying changes from dripping to multi-jet mode.

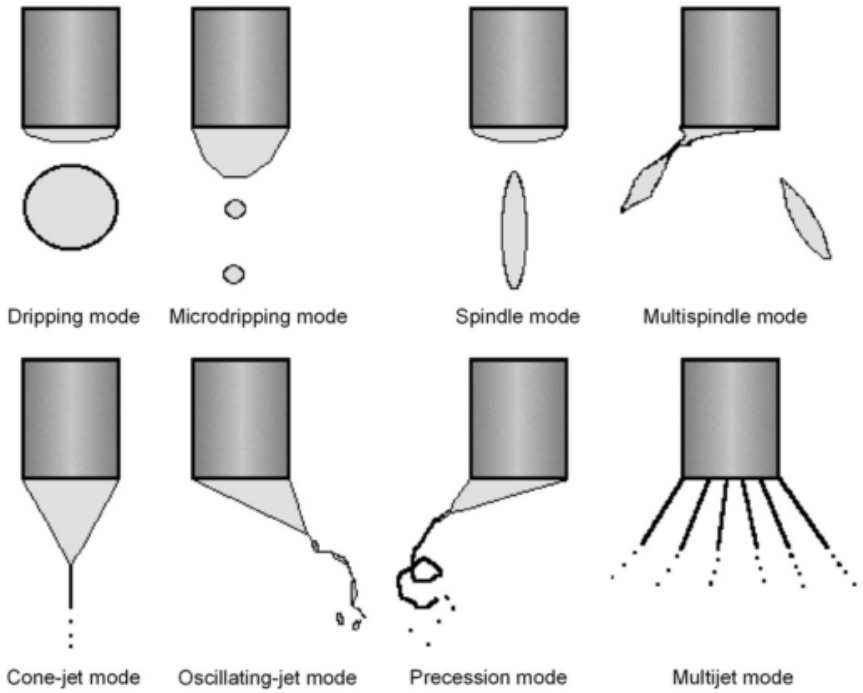

Figure 8. Main modes of electrospraying [57].

The needle tip can be of any diameter and shape. Blunt tipped capillaries provide the most uniform and smooth thin films [58]. Beveled tips (hypodermic needles) and saw-tooth nozzles allow the Taylor Cone-jet to operate over a wider voltage and flow rate range, leading to great cone stability [58,59].

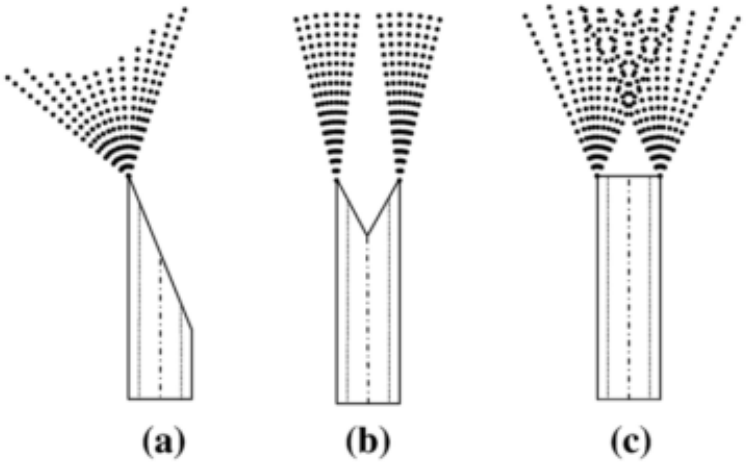

Figure 9. Typical electrospray capillaries: a) beveled (hypodermic), b) saw-toothed, c) blunt tipped capillary in multi-jet mode [58].

Standard capillary/substrate setups (Figure 10a) are often modified in order to improve the deposition properties of the electrosprayed film. The largest disadvantage of the capillary/substrate setup is that the substrate serves as an active electrode and needs to be conductive in order to remove charges gained from charged droplets. In order to reduce electrical charge buildup on the substrate additional electrodes of circular symmetry (Figure 10b) are used in-between the capillary and the substrate. These circular electrodes are either maintained the same potential as the capillary, grounded, or held at intermediate potentials in order to create convergent electric field lines. These electrodes can also focus the spray to a smaller area, or to create deposition patterns [45,57,60].

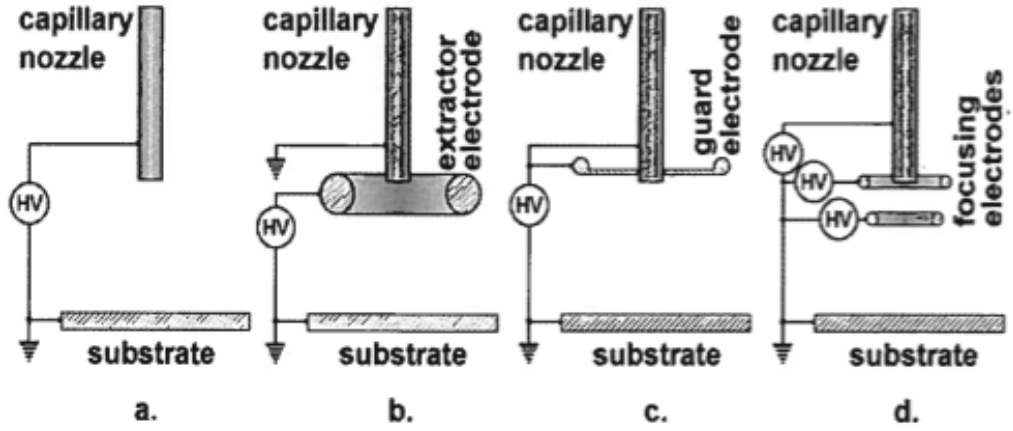

Figure 10. Various configurations of electrospray systems with circular electrodes [45].

Systems with down facing spray capillaries can use either a pump or gravity to induce a flow rate through the nozzle. The major disadvantage to this set up is that gravity can tend to pull large droplets onto the substrate without undergoing electrical nebulization. Reverse configured set ups utilize an upward facing nozzle, and horizontal facing capillaries have been used in thin film deposition set-ups [61,62]. In these set-ups

gravity pulls larger droplets to the ground while fully atomized droplets are accelerated by the electric field to the deposition substrate.

3.2.1 Formation of Electrospray Jet and Droplets

Electric potential applied to a liquid filled conductive capillary causes the liquid to deform based on a balance of bulk forces (equation 3.2) and normal and tangential surface tension forces (equation 3.3) on the liquid. This leads to the elongation of the liquid meniscus at the tip of the capillary (Taylor Cone) to the formation of a jet, which later breaks into droplets (Figure 11).

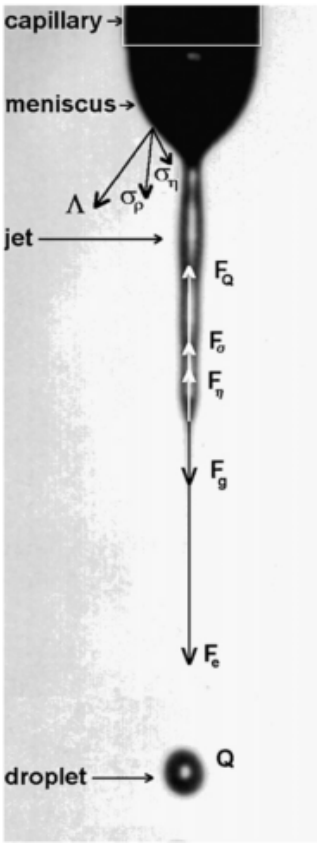

Figure 11. Force balance schematic of a liquid being electrosprayed in cone-jet [57].

Equation 3.2 describes the balance of bulk forces per unit volume on the liquid [63]:

$$\frac{\partial \rho_l \vec{v}_l}{\partial t} = \vec{L}_g + \vec{L}_l + \vec{L}_\rho - \vec{\Phi}_d - \nabla \bullet \left(\vec{\vec{\Pi}}_{\Delta p} + \vec{\vec{\Pi}}_\eta + \vec{\vec{\Pi}}_\rho \right) \qquad (3.2)$$

While equation 3.3 describes the stress balance onto the surface of the liquid [63]:

$$\nabla \times \vec{\vec{\Xi}} = \vec{\vec{\Pi}}_{\Delta p} + \vec{\vec{\Pi}}_{\eta} + \vec{\vec{\Pi}}_{\rho} + \vec{\vec{\Lambda}}_{l} \qquad (3.3)$$

Where ρ_l is the density of the liquid and v_l is the velocity of the liquid jet, and Ξ is the surface tension tensor of the liquid that opposes the tensors causing deformation. Components L_g, L_l, L_ρ, and Φ_d are forces per volume density, while $\Pi_{\Delta p}$, Π_η, Π_ρ, and Λ_l are stress tensors describing deformation of the liquid. These components are described as follows:

In a continuous medium, the electrodynamic force (L_l) can be represented by the volume density of forces on a finite volume of liquid [45]:

$$\vec{L}_l = \rho_q \vec{E} + \frac{1}{2}\left[\vec{D}\nabla^T \vec{E} - \vec{E}\nabla^T \vec{D}\right] \qquad (3.4)$$

Where ρ_q is the volume charge density, E is the localized electric field, and D is the electric flux density. The electrodynamic force is caused by the electric field (F_e) generated from the voltage applied to the capillary, and point charge force (F_Q) caused by attraction/repulsion from previously emitted droplets.

Forces from gravity and inertia are also expressed in terms of volume density. The gravitational force volume density (L_g) and inertial force volume density (L_ρ) are as follows [45]:

$$\vec{L}_g = \rho_l \vec{g} \qquad (3.5)$$

$$\vec{L}_\rho = \rho_l \frac{dv_l}{dt} \qquad (3.6)$$

The drag force volume density (Φ_d) is caused by air resistance on the jet:

$$\vec{\Phi}_D = \frac{c_x \rho_a}{2V}\left(\vec{S}\vec{v}\right)\vec{v} \qquad c_x = \frac{24}{\mathrm{Re}} f\left(\mathrm{Re}\right) \qquad (3.7)$$

Where V is the liquid volume, v is the liquid velocity, ρ_a is the density of air, and Re is the Reynolds number.

The stress tensors on the liquid surface deform the liquid's shape and are opposed to the surface tension tensor (Ξ) of the liquid. The stress tensors from equations 3.2 and 3.3 are defined below:

The electrodynamic stress tensor (Λ_l) is caused from the surface charge density and the local electric field:

$$\vec{\vec{\Lambda}}_l = \vec{q} \otimes \vec{E} + \vec{\vec{1}} * \frac{1}{2}\left[\vec{D}(\vec{E}_l - \vec{E}_g) - \vec{E}(\vec{D}_l - \vec{D}_g)\right] \qquad (3.8)$$

Where E is the local electric field, D is the electric flux density, and $\otimes$ denotes the dyadic product of two vectors. The subscript *l* refers to the liquid and the subscript *g* refers to open space where liquid is not present.

The pressure stress tensor ($\Pi_{\Delta p}$) is caused by the static pressure difference on both sides of the interphase surface is defined as:

$$\vec{\vec{\Pi}}_{\Delta p} = \vec{\vec{1}}\left(p_l - p_g\right) \qquad (3.9)$$

Where p_l is the pressure of the liquid and p_g is the pressure of the local air.

The liquid dynamic viscosity stress tensor (Π_η) is proportional to the gradient of liquid velocity and perpendicular to the interphase surface.

$$\vec{\vec{\Pi}}_\eta = \eta_l \nabla \vec{v}_l \qquad (3.10)$$

Where η_l is the liquid viscosity and v_l is the liquid velocity.

The liquid inertia stress tensor (Π_ρ) is proportional to the liquid density and is the dyadic product of local liquid velocity at the interphase surface.

$$\vec{\vec{\Pi}}_\rho = \rho_l \vec{v}_l \otimes \vec{v}_l \qquad (3.11)$$

Once the charge accumulated in the Taylor Cone exceeds the surface tension forces (the Rayleigh Limit), a small jet is formed at the tip of the Taylor Cone. The jet will then disrupt into two different types of instabilities: varicose or kink, and can be continuous or sporadic [64].

Equations 3.2 and 3.3 are theoretical equations balancing electrodynamic and surface tension forces on finite liquid volumes and are yet to be solved for the general case of cone-jet mode. The mode of spraying transitions from cone-jet mode to other spray modes (Figure 8) as the electric potential applied to the capillary and/or the volumetric flow rate of the liquid is adjusted. Theoretical models of these transitions are yet to be analytically explained [45,57].

The average size of the droplets emitted from electrospray nebulization in the cone-jet mode has been determined from the scaling laws of theoretical analysis [65–69] and confirmed by many experimental results [65,70,71]. Equation 3.12 expresses the mean droplet size of an electrosprayed droplet:

$$d = \alpha\left(\frac{Q^{aQ}\varepsilon_0^{\,a\varepsilon}\rho_l^{\,a\rho}}{\sigma_l^{\,a\sigma}\gamma_l^{\,a\gamma}}\right)^{1/3} \qquad (3.12)$$

where α is a constant dependent upon spray conditions and liquid permittivity, Q is the liquid flow rate, γ_l is the liquid conductivity, ε_0 is the permittivity of free space, and ε is the dielectric constant of the liquid. The exponents in equation 3.12 vary depending on the author, and are stated in Table 1.

Table 1. Constants for variables in equation 3.12 to determine mean droplet size.

Authors	aQ	$a\varepsilon$	$a\rho$	$a\sigma$	$a\gamma$
Fernandez de la Mora and Loscertales [1994]	1	1	0	0	1
Ganan-Calvo [1999] and Ganan-Calvo et al. [1997]	3/2	1/2	1/2	1/2	1/2
Hartman et al. [2000]	3/2	1/2	1/2	1/2	1/2

By examining equation 3.12, it can be concluded that the droplet size may be decreased by decreasing the liquid flow rate and increasing the liquid's conductivity or surface tension. Equation 3.12 does not consider capillary diameter, electric potential, or liquid viscosity.

The droplets' diameter dependence on the voltage in dripping mode is give by equation 3.13 [72]:

$$d(U) = d_0\left(1-\left(\frac{U}{U_{crit}}\right)^2\right)^{1/3} \qquad (3.13)$$

where d_0 is the droplet diameter when U=0, and U_{crit} is the onset voltage of cone-jet mode. The onset voltage (U_{onset}) for the cone-jet mode is described as a balance of the electrical forces and the surface tension forces [73]:

$$U_{onset} = A\left(\frac{d_c\sigma_l}{\varepsilon_0}\cos\theta\right)^{1/2}\ln\frac{4d}{r_c} \qquad (3.14)$$

where d_c is the inner capillary diameter, d is the droplet diameter, σ_l is the surface tension of the liquid, and θ is the half angle of the Taylor Cone at the capillary outlet.

The minimum flow rate required for the cone-jet mode to operate in steady state is given by equation 3.15 [74]:

$$Q_{\min} \approx \frac{\sigma_l\varepsilon_0\varepsilon}{\rho_l\gamma_l} \qquad (3.15)$$

where γ_l is the conductivity of the liquid. If the liquid's electrical conductivity is 10^{-3} S/m then the size of the droplets can be on the order of 1 um. The size of the droplets decreases to about 10 nm when the electrical conductivity is approximately 1 S/m [74].

In this work, the mode of electrospray best suited (determined by our own experimentation) for thin film deposition of water soluble polymers occurs near the end of cone-jet mode, but before the transition to oscillating-jet mode. This is marked largely by the absence (or near absence) of the 'jet' and the Taylor Cone's apex being the initial point of droplet formation. The droplets immediately begin separating in a spherical cloud due to coulombic repulsion from other droplets. The expansion of a spherical cloud of charged droplets is given by equation 3.16 [75]:

$$-\frac{1}{c_d}\frac{dc_d}{dt} = \frac{2C_c\varepsilon_0 c_d E^2{}_{ds}}{\eta\rho_l} = \frac{c_d}{\tau_{\exp}} \tag{3.16}$$

where c_d is the mass concentration of the droplets, η_g is the gas dynamic viscosity, and C_c is the Cunningham slip correction factor. E_{ds} is the electric field on the surface of a single droplet charged to a magnitude of Q_d [75]:

$$E_{ds} = \frac{Q_d}{4\pi\varepsilon_0 r^2} \tag{3.17}$$

From equation 3.16, τ_{exp} is the time constant of expansion of the cloud [75]:

$$\tau_{\exp} = \frac{\eta_g\rho_l}{2C_c\varepsilon_0 E^2{}_{ds}} \tag{3.18}$$

The mass concentration of the cloud decreases reciprocally with time as the cloud expands [75]:

$$c_d = c_{d0}\left(1 - \frac{t}{\tau_{\exp}}\right) \tag{3.19}$$

The spray parameters are of primary importance in the deposition of thin solid films. Furthermore, it should be noted that the deposition of a charged particle on a grounded substrate is more effective than for an uncharged particle [45].

Charged droplets formed from an electrospray system can also undergo fission as they travel from the point of formation to the substrate. The solvent of the droplets evaporates as the droplets travel along the axis to the substrate for deposition. As the solvent evaporates from the droplets, the size of the droplets decreases, this increases the charge to volume ratio. When the charge to volume ratio increases to about 90% of the Rayleigh Limit the droplet ruptures into two droplets of uneven sizes [49,76]. The initial droplets' diameters are relatively uniform and assumed to be spherical. Alessandro and Tang, showed that as droplets travel along the spray axis, their diameter decreases in a uniform fashion until rupture occurs, and then an array of different sized droplets are in the spray stream as shown in Figure 12. Smith et al. measured the average diameter and charge (also shown as a percentage of the Rayleigh Limit in Figure 13) of water droplets as a function of time. The sudden decreases in charge indicate when fission occurs due to increased charge-to-volume ratio from solvent evaporation.

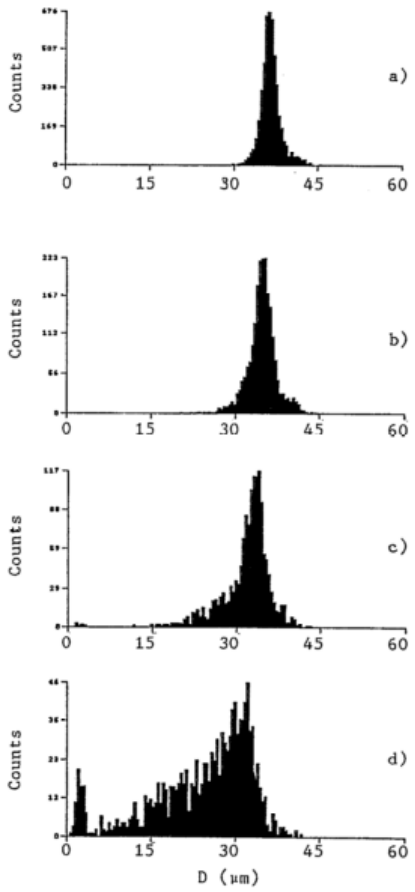

Figure 12. Size distribution of electrosprayed droplets moving on the order of 2-3 m/s along the spray axis: (a) z=7.6 mm (b) z=25.8 mm (c) z=33.6 mm (d) z=43.6 mm. z-axis origin is at the outlet of the capillary [49].

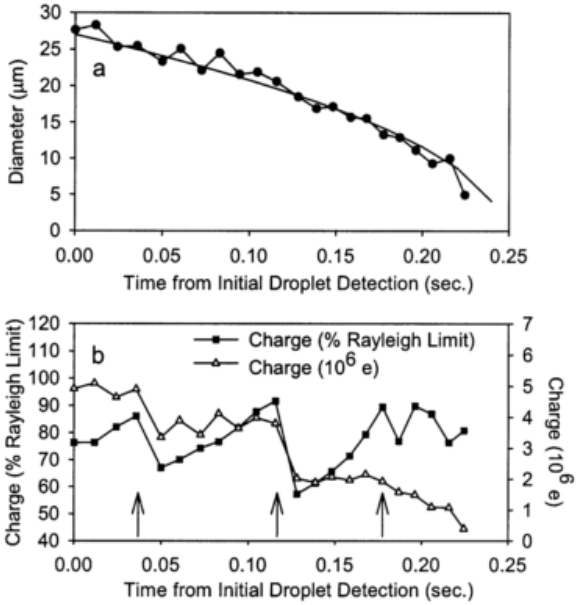

Figure 13. Evaporation and discharge of electrosprayed water droplets at 43.9°C (110°F) in nitrogen buffer gas. (Top) Variation of droplet diameter with time. The smooth line represents the predicted evaporation dynamics of a water droplet in vapor-free nitrogen gas at 43.9°C. (Bottom) Variation of droplet charge with time, represented as the number of elementary charges and as the percent of the Rayleigh limit of charge for measured droplet. Arrows indicate coulombic particle fission which occur around 90% [76].

Relative humidity of the air also effects the formation of droplets and their deposition. Excess humidity slows the evaporation process of the droplets, which also inhibits fission of particles as they dry. Not much characterization regarding the effects of humidity on the formation of droplets in cone-jet mode has been done. Through our observations, air of higher humidity requires a greater electric voltage to create a Taylor Cone. Regardless of humidity, Taylor Cones of a higher potential are less stable.

This work utilizes electrospray of liquids for thin film deposition near the end of cone-jet mode, but before the transition to oscillating-jet mode. Operation in this mode of electrospraying has been the most successful at achieving uniform thin films with steady Taylor Cones. The end of cone-jet mode is noticeable by the absence (or near

absence) of the 'jet', making the Taylor Cone's apex the initial point of droplet formation.

3.3 Application to Polymer Solar Cells

Polymer solar cells (PSCs) have almost exclusively been fabricated by using the spin coating technique to deposit a thin film of the organic polymer and C_{60} derivative. There are two major disadvantages of the spin coating technique for the fabrication of PSCs that can be overcome by using Electrospray Deposition (ESD): the inability for high throughput and the dissolution of previous layers by the spin coated solution's solvent. ESD has the potential to significantly increase the total yield of PSC area while using less material. ESD can be set up so there is minimal wasted polymer. Whereas during spin coating a large amount of polymer is lost due to the non-recyclable polymer displaced from the high rotational speeds.

The most commonly reported/researched polymer solar cell structure is ITO/PEDOT:PSS/(Polythiophene + C_{60} derivative)/Al. The hole conducting layer PEDOT:PSS (poly(3,4-ethylenedioxythiophene) poly(styrenesulfonate)) is a suspension of PEDOT:PSS in water. When spin coating a water-soluble polymer onto the PEDOT:PSS, it is extremely difficult to avoid dissolution of the PEDOT:PSS layer. ESD is advantageous when creating multiple layers from a common solvent since the particles are nearly dry upon deposition. ESD is also more economical than other common deposition methods such as chemical vapor deposition, physical vapor deposition, or magnetic/RF sputtering [57].

The first polymer solar cell created with an ESD active layer was by Kim et al. in 2010. They utilized ESD to fabricate a bulk heterojunction active layer consisting of

poly(3-hexythiophene) (P3HT) and C_{61}-butyric acid methyl ester (PCBM). Their final device structure was ITO/PEDOT:PSS/(P3HT:PCBM)/Al and achieved a maximum efficiency of 3.25%. The solution used for ESD was 1% wt concentration of P3HT:PCBM (1.2:1) in a mixture of chlorobenzene and tetrachloroethane. After ESD, the active layer was subjected to solvent vapor soaking (SVS) in chlorobenzene for 1 hour at room temperature. The SVS treatment successfully rewelded the interfacial boundaries among the deposited particles as seen in Figure 14. Impedance spectroscopy analysis revealed that the series resistance of the PSC was significantly reduced after SVS treatment. Spin coated PSCs fabricated under identical conditions achieved an efficiency of 3.62% [77].

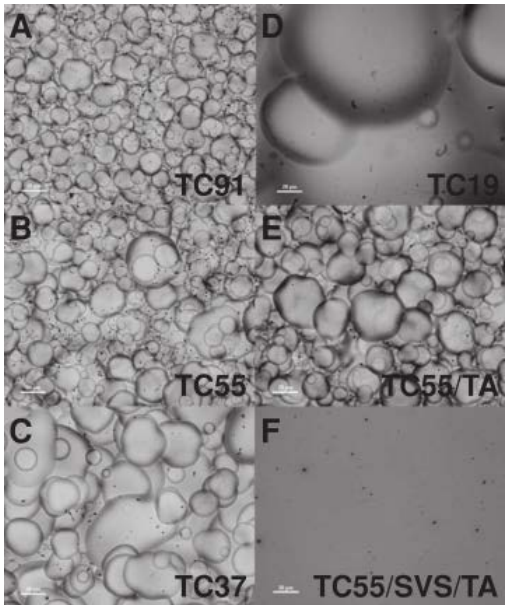

Figure 14. Optical microscope images (x600) of the ESD P3HT:PCBM active layer onto PEDOT:PSS coated ITO/glass. A-D) show the ESD films from various mixtures of tetrachloroethane:chlorobenzene ratios of A) 90:10, B) 50:50, C) 30:70, and D) 10:90. E) Film B after thermal annealing at 160°C for 15 min. F) Film B after SVS treatment in chlorobenzene followed by thermal annealing at 160°C [77].

Another approach taken to reducing the surface roughness of polymer thin films from ESD is by mixing acetone into the solvent. Fukuda et al. reported in 2011 the

reduction in surface roughness of ESD of P3HT thin films from solutions in dichlorobenzene by mixing 5%, 10%, 15%, and 20% acetone by volume. The root mean square (RMS) surface roughness of the thin films from the aforementioned solutions were 3.70, 63.8, 33.1, and 2.63 nm as shown in Figure 15. The power conversion efficiencies for 10% and 15% were quite low while the efficiency of the 20% solution was 1.9%, which wasn't far from the spin coated device's efficiency of 2.7%. During the ESD of the thin films, the spray plume's diameter was measured 6 mm from the tip of the spray capillary. The plume's diameter increased linearly from about 1mm at 5% concentration to approximately 6.2 mm at 20% concentration. The relative dielectric constant of acetone (20.7) compared to dichlorobenzene (9.9) causes the plume diameter to increase as the concentration of acetone increases. They concluded that the addition of acetone caused the formation of smaller particles from the Taylor cone, which dried more quickly. In the case of the 5% concentration, there wasn't enough acetone to fully dry them before deposition leaving the thin film largely unaffected. For 10% and 15%, the particles dried while they were still aggregated. A threshold was met in the case of 20% where the spray plume's diameter increased enough to break down the aggregates to much smaller sized particles, which were fully dried upon deposition for a much smoother film [78].

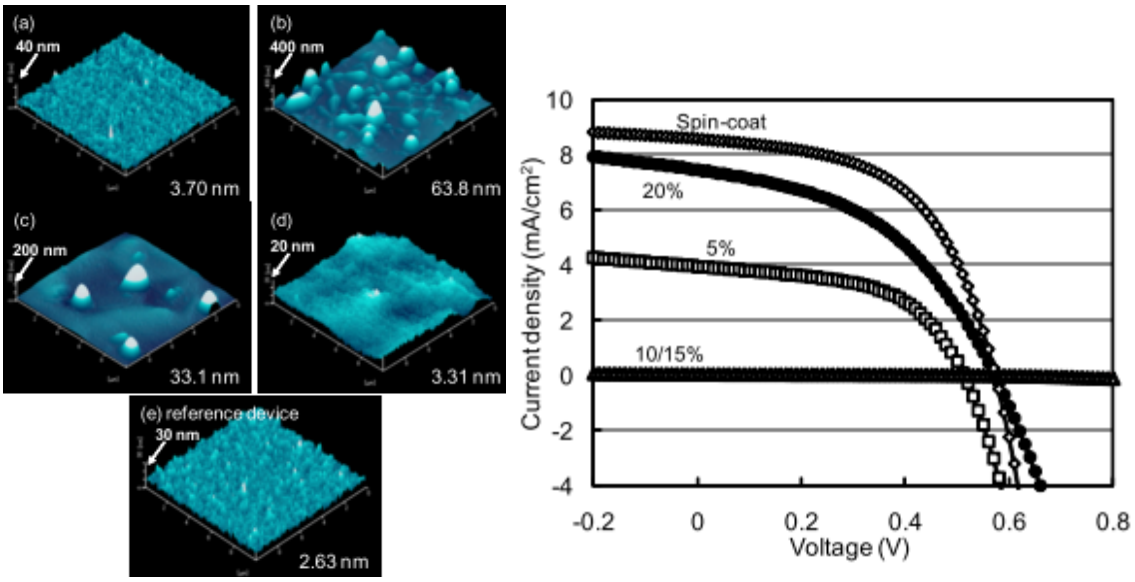

Figure 15. (Left) AFM images of the P3HT:PCBM layers from ESD. Concentrations of acetone were (a) 5, (b) 10, (c) 15, (d) 20 volume %. (Right) J-V curves showing that the 20% acetone by volume performed the best [78].

There are many other applications of electrospray deposition of thin films besides fabrication of PSCs. Organic light emitting diodes (OLED) have been fabricated from electrospray technology [79]. ESD of a polymer electrolyte, yttria stabilized zirconia thin film in solid oxide fuel cells (SOFC) is a trending topic in fuel cell research due to the ability to create films thinner than 10 microns [61]. ESD has also been used for fabrication of both electrodes as well as the polymer electrolyte in SOFC making complete fabrication a one step process by merely changing solutions [80]. In lithium ion batteries, the conductivity of the solid electrolyte can be increased two orders of magnitude by creating porous electrodes via ESD [81].

4. MATERIALS

This chapter will give a brief overview of the chief materials used in creating the PSC devices in this work. The chief materials include the water soluble polymer PTEBS, C_{60} tris-acid, and TiO_2. Materials used for the electrodes (gold and aluminum) are not discussed in this section due to their limited functionality. Their work functions should align properly within the theoretical flow of electrons determined by the device's structure. Device structures and energy band diagrams are presented in the following chapter.

4.1 PTEBS

The water soluble polymer used in this work is (sodium poly[2-(3-thienyl)-ethoxy-4-butylsulfonate], also known as PTEBS (Figure 16). PTEBS is water soluble due to the sodium sulfonate tail attached to the end of the polythiophene base which separates in the presence of water's strong polarity. PTEBS is responsible for absorbing light and the absorbed light excites electrons into the LUMO or conduction band of the PTEBS. UV-Vis absorption data of the PTEBS is shown in Figure 17. The PTEBS used in this study was purchased from QCR Solutions [82].

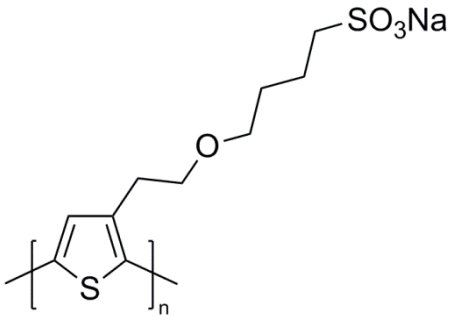

Figure 16. Chemical structure of the water soluble polythiophene PTEBS.

The UV-Vis absorption spectrum of PTEBS is illustrated in Figure 17. The peak of the absorption curve is at approximately 430 nm. The band gap is estimated to be

approximately 2.0 eV due to the onset of absorption around 610 nm. Cyclic voltammetry measurements of PTEBS thin films by Tran-Van et al. show oxidation onset occurs between +0.3 and +0.4 V vs. saturated calomel electrode (SEC) [83]. The HOMO level of PTEBS can be estimated at the onset point of absorption using an adjustment factor of 4.4 to 4.7 eV to convert the energy values from SCE to energy values in a vacuum. Thus, an estimate of the HOMO level can be estimated to be between -4.7 and -5.1 eV. With an estimated optical band gap of 2 eV, the LUMO would be between -2.7 and -3.1 eV. Qiao et al. reported PTEBS HOMO values of -5.0 and -5.3 eV and LUMO values between -2.8 and -3.1 [84].

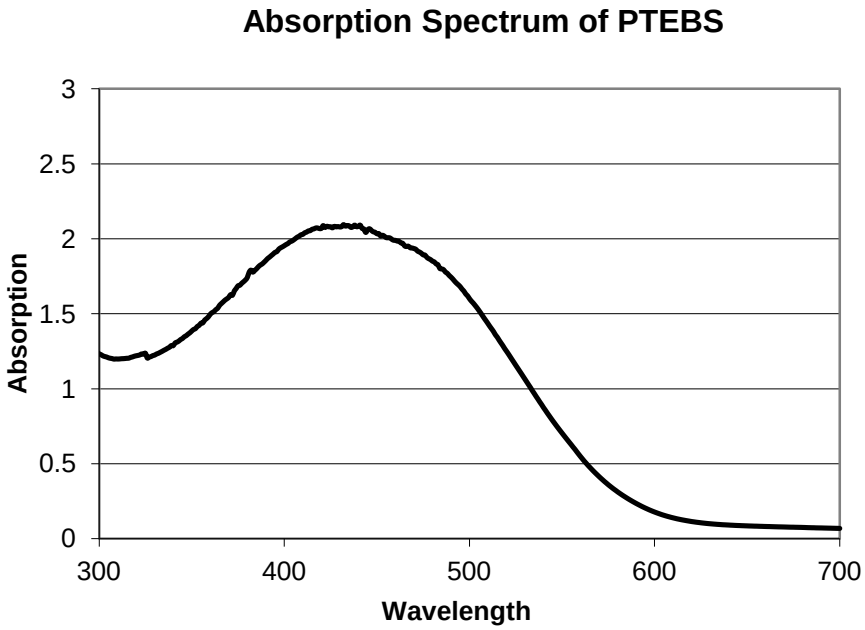

Figure 17. Absorption spectrum of a spin coated PTEBS thin film taken from a Lambda 40 UV-Vis spectrometer.

4.2 C_{60} Pyrridoline tris-acid

Fullerene, or C_{60} molecules, are not readily soluble in anything. Chemical engineering of fullerenes by adding ionic tails creates soluble fullerenes. The most common organic soluble fullerene investigated in PSCs is [6,6]-phenyl-C_{61}-butyric acid

methyl ester (PCBM) [30]. The water soluble fullerene derivative investigated in this work (Figure 18): C_{60} Pyrridoline tris-acid (referred to as C_{60} tris-acid). This water soluble fullerene has never been previously reported for PSC device fabrication. However, other water soluble fullerene derivatives have successfully been used [44,85,86]. The LUMO levels are estimated to be in the range of -3.7 eV and -4.7 eV which is similar to C_{60} and PCBM [85–88].

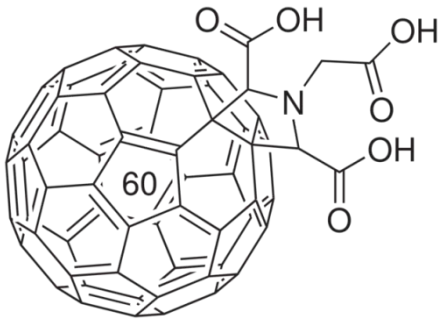

Figure 18. Chemical structure of C_{60} Pyrridoline tris-acid [89].

4.3 TiO_2

Titanium dioxide (TiO_2) is an inorganic semiconductor that is cheap, safe, and chemically inert. The TiO_2 layers were formed from Degussa P25 TiO_2 nanopowder consisting of 70% anatase and 30% rutile particles in a suspension of 0.01 M acetic acid. Highly porous nanostructures with large surface areas easier to fabricate from anatase particles [90]. The nanoparticles have an average diameter of 25 nm. When the homogenous solution of suspended TiO_2 nanoparticles is dried, it forms a porous inner penetrating TiO_2 network of loosely packed nanoparticles. The average pore size ranges from 20 to 100 nm [41].

TiO_2 films only absorb in the ultraviolet region and do not absorb light in the visible region as shown in Figure 20. Therefore, TiO_2 is a suitable inorganic material of

PSCs since it allows light which is absorbable by the polymer to pass through. The energy band gap is approximately 3.2 eV which is obtained from the absorption onset at 385 nm. The LUMO and HOMO energy levels are -4.2 ev and -7.4 eV, respectively. TiO_2 films function as effective electron acceptors in PSC devices because of their high electron mobility of 0.1 cm^2/Vs [91].

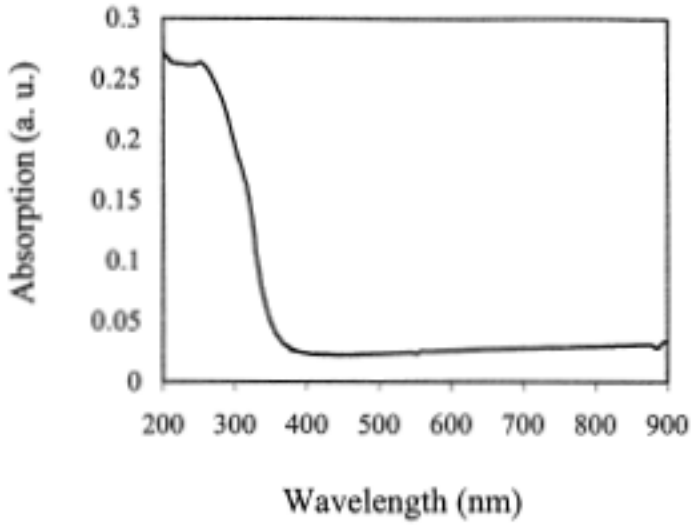

Figure 19. Absorption spectrum for TiO_2 layer [92].

5. CHARACTERIZATION OF WATER SOLUBLE PTEBS POLYMER THIN FILMS BY ELECTROSPRAY DEPSOTION

In this chapter we have developed and characterized thin films of PTEBS from ESD for use in polymer solar cells (PSCs). PTEBS thin films deposited by spin coating and drop casting have successfully been used as the electron donor in the fabrication of PSCs [40,41,93–97]. Water soluble polymers are advantageous in that their solvent is cheap and environmentally friendly. Water soluble polymer thin films have also been used in the fabrication of organic transistors [98,99], LEDs [100], and fluorescent CdTe/polymer films [101]. The aim of this study is to understand the evolution of thin, nanoscale films from charged electrospray aerosols.

5.1 Parameter optimization

Many different parameters were tuned so that a stable Taylor Cone could be held indefinitely and that particles were still slightly wet upon deposition. An unstable Taylor Cone results in a loss of the spray plume and large droplets of fluid deposit on the substrate causing dissolution of previously deposited PTEBS. Taylor Cones must also be stable for extended periods of time in order to ESD thin films of the proper thickness. Efficient solar cells need active layers approximately 150 nm so that they are thick enough to be able to absorb a significant amount of light, but thin enough to reduce high recombination rates due to the polymer's low carrier mobility [32,33]. A PTEBS sample fabricated via ESD for 1.5 hours with a flow rate of 2 ul/min produced a film approximately 200 nm thick. Therefore, a Taylor Cone needs to be stable for at least 2 hours, even longer if depositing at a slower flow rate.

5.1.1 Effect of Solvent Properties

It was determined that electrospraying any concentration of PTEBS polymer dissolved in pure de-ionized water was unfeasible. The surface tension of the water was too much to overcome to get a stable Taylor Cone. Once the voltage surpassed the Rayleigh Limit, sporadic spitting of large droplets occurred.

Two different surfactants, sodium lauryl sulfate (SLS) and ammonium lauryl sulfate (ALS), were experimented with to decrease the surface tension of de-ionized water to make ESD of water feasible. ALS was the preferred surfactant because it was a liquid and expected to be fully evaporated from the thin film after ESD, while the SLS was a fine powder that could contaminate the solar cell's active layer. Concentrations of 0.5%, 1%, and 5% were unsuccessful with both surfactants. The ALS also tended to separate in the syringe as time progressed leaving a thicker/denser fluid layer at the bottom.

Ethanol was chosen instead of a surfactant to lower surface tension of the solution to be sprayed because it is cheap, safe, and highly miscible with water. By adding ethanol to the solvent we were able to obtain a steady Taylor Cone during ESD. The more ethanol in the solvent the more stable the ESD performed. A 50:50 ratio of water to ethanol has been selected the best solvent due to great stability and consistency, while keeping true to the green motives of using water-soluble polymers. Thin films produced from this solvent with 0.5% weight concentration of PTEBS, and electrosprayed at 6.5 – 7.5 kV were very uniform. However, the film density didn't seem to be as high as a spin-coated film. The film was easily destroyed by gentle touch and resembled a fine coating of powdered sugar on a doughnut. Thermal annealing of the film at 150°C had no effect.

Moving the substrate closer to the nozzle to reduce evaporation time in the air should be considered.

It appears that a dense thin film (similar to one that would be spin coated) is the ideal morphology of an electrosprayed thin film for polymer solar cells. Film porosity is often the result of fast evaporation of the solvent. Ethanol is very volatile and being 50% of the solvent, it is likely that particles are nearly dry upon deposition. Butyl carbitol is a common additive used when electrospraying with ethanol. Since its boiling point of 231°C prevents fast droplet evaporation compared to ethanol's boiling point of 78°C. Chen et al. reported that electrospraying butyl carbitol with ethanol at a 50:50 ratio resulted in semi-dry particles converging together on the substrate to form a dense uniform layer. Lower concentrations of butyl carbitol (15:85 volume ratio) resulted in a reticular structured particles closely packed together to make a film [102].

5.1.2 Nozzle Type and Spray Modes

Needle size (internal diameter) directly affects the type of stable spray attainable for a given solution. A 0.5% solution of polymer in water and ethanol (1:1 ratio) is unable to sustain a single steady Taylor Cone in large needle sizes, but can have multiple stable Taylor Cones. Multiple stable Taylor Cones produce a great spray however a pattern forms on the deposition substrate. To overcome the pattern and create a smooth thin film the substrate needs to be in constant motion within the spray plume. A moving grounded electrode adds complexity to the ESD process. Attempts to create a moving grounded electrode failed because the Taylor Cones would become unsteady since the electric field lines weren't constant. This was a limitation of available equipment.

Therefore, the smallest needles tested thus far, 30 gauge (108 microns), provide the most stable Taylor Cones in single jet mode.

The shape of the needle tip also affects the stability of the Taylor Cone. Blunt tipped needles fared well at maintaining a Taylor Cone, but a hypodermic needle (beveled tip) provides much more stability. This is due to the geometry of the needle having a fine tip on only one side. A Taylor Cone is able to form at the tip and is much smaller than a Taylor Cone formed around the entire inner diameter of a blunt tipped needle. The 30 gauge hypodermic needle also provided more stability than a handmade stretched glass tip.

5.1.3 Flow Rate

The necessary flow rate for steady state electrospray should equal the volume of droplets displaced from the apex of the Taylor Cone so that the Cone maintains a constant volume. The flow in the ESD process is not driven by the syringe pump, it is an electrostatically driven process. Higher voltages will spray greater volumes, but the voltage can't exceed a certain threshold or the spray mode will rapidly transition to multi-jet mode. It has been found that a flow rate of 0.5 – 2.5 microliters per minute is the optimum flow rate range for maintaining a steady Taylor Cone.

5.1.4 Solution Concentration

Solution concentration is directly proportional to the surface tension of the liquid and particle size upon deposition [45]. Therefore, solutions with low concentrations of polymer lead to lower surface tensions and smaller particle size. Low concentrations increase the duration of ESD required to form a thick enough layer. Our research shows that concentrations less than 0.5% spray nearly identical to pure solutions (spraying only

the solvent). A 0.5% concentration is able to produce a thick enough (200 nm) in less the 1.5 hours, which appears to be a reasonable amount of time.

5.1.5 Solvent Vapor Soaking

Solvent vapor soaking (SVS) is a technique used to control internal and external morphologies of thin films from ESD in PSCs [77]. SVS is the term for exposing the ESD to the solvent vapor for an extended period of time. The solvent vapor gently dissolves the particles and welds their interfacial boundaries back together. This method has briefly been investigated by filling an oven full of steam and then introducing the substrate. Condensation of the steam ruined the film.

5.2 Experimental

Transparent conductive FTO (fluorine doped tin oxide) coated glass substrates of 8 – 12 Ω sheet resistance were purchased from Hartford Glass Company. A highest grade V1 AFM mica disc (purchased from Ted Pella) was then adhered to the center of the FTO glass substrate. The mica disc was cleaved immediately before sputtering with a 2.7 nm platinum film.

The water-soluble polythiophene PTEBS was purchased from QCR Solutions. A stock solution of PTEBS was created by dissolving in DI water at a concentration of 2% by weight. The solution was stirred for three days at room temperature. Water and ethanol were added to dilute the stock solution to 0.5% with a solvent ratio of 1:1. The diluted solution was then sonicated for 15 minutes immediately before being loaded into a 1 ml syringe with a 30 gauge hypodermic needle.

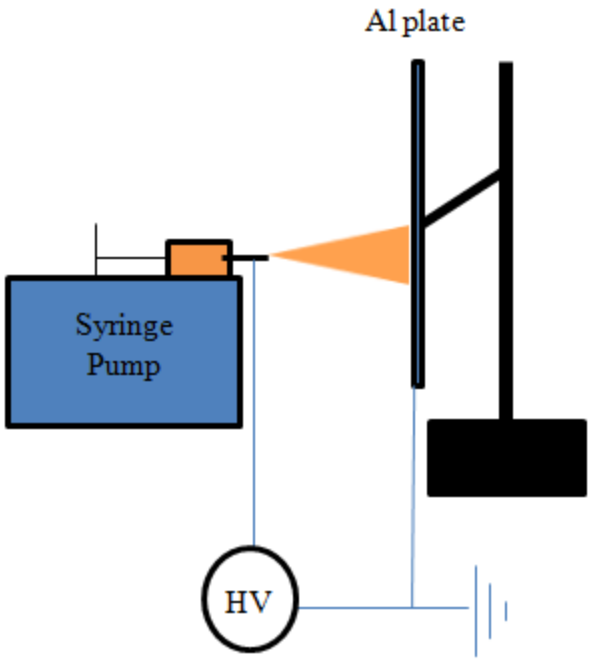

Figure 20. Schematic of horizontal ESD apparatus used in experiments.

Figure 21 is a schematic of the horizontal electrospray configuration used to deposit the PTEBS thin films. The distance between the needle tip and the grounded aluminum plate was 10 cm. The flow rate through the needle, controlled by a syringe pump, was 1.5 μl/min and the applied voltage was 8 – 9 kV. The FTO substrate was grounded to the aluminum plate using copper tape before the syringe pump and voltage were activated. Films were analyzed using a Veeco Icon Dimension AFM, Ambios XP-1 profilometer, and a Lambda 35 UV-Vis spectrometer.

5.3 Results and Discussion

One of the most important requirements for creating a uniform thin film from ESD is to maintain a stable Taylor cone at the tip of the spraying capillary. Steady Taylor cones result from the proper balance of the following parameters (achieved at the values listed above): distance between spray tip and grounded substrate, flow rate through the needle, applied voltage, and solution properties. Interruptions in steady flow from the tip

of the Taylor cone can result in the emission of large droplets which degrade film quality. Ethanol was added to the solution to reduce the liquid surface tension compared to a pure water solution. A solution concentration of 0.5% was found to result in good Taylor cone stability. The syringe pump flow rate was adjusted to replenish the fluid removed by the aerosol and such that the ESD process remained electrostatically driven. The applied voltage was varied between 8 – 9 kV depending on the flow rate and distance between the needle and grounded substrate. A distance of 10 cm was determined to be optimal for thin film fabrication due to the amount of time needed for evaporation of the solvent in droplets. The voltage was increased from 0 kV and held constant once a stable Taylor cone was present at the tip of the beveled edge of the hypodermic needle (Figure 22). Ksapabutr et al. also reported Taylor cone stability at the orifice of the nozzle apex [58].

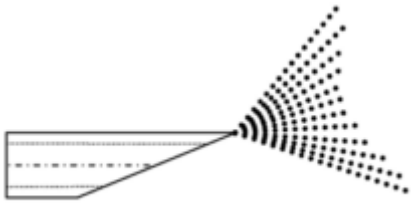

Figure 21. ESD spray formation from 30 G hypodermic needle [58].

Figure 23 shows optical microscope images of PTEBS thin films from ESD where an unstable (left) and a stable (right) Taylor cone were maintained for the duration of the deposition. An unsteady Taylor cone resulted in the spitting of large droplets (orders of magnitude larger) from the spray capillary. The large droplets would dissolve the previously deposited film upon deposition and displace the PTEBS in circular rings. A stable Taylor cone created films free of large defects due to the constant deposition of smaller droplets.

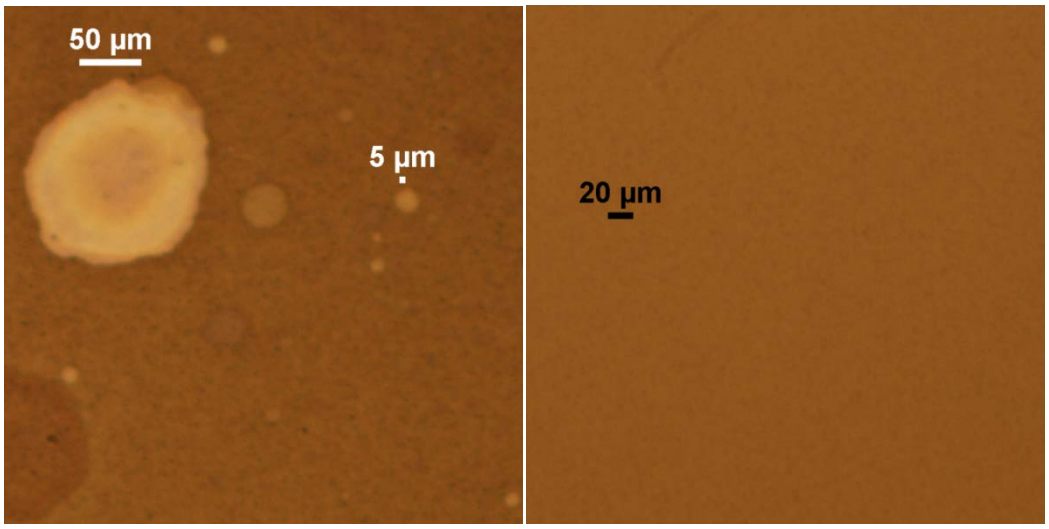

Figure 22. Optical microscope image at 10x of PTEBS films where a Taylor cone was (left) unstable and (right) stable.

AFM characterization of films from ESD was carried out on cleaved mica discs adhered to FTO coated glass (Figure 24) to provide a flat substrate to analyze particle size and film roughness. Prior to electrospraying the polymer, the cleaved mica was sputtered with a 2.7 nm thick layer of platinum to create the conductive surface necessary for ESD. The platinum covered mica had a root mean square (RMS) surface roughness of 87.3 pm.

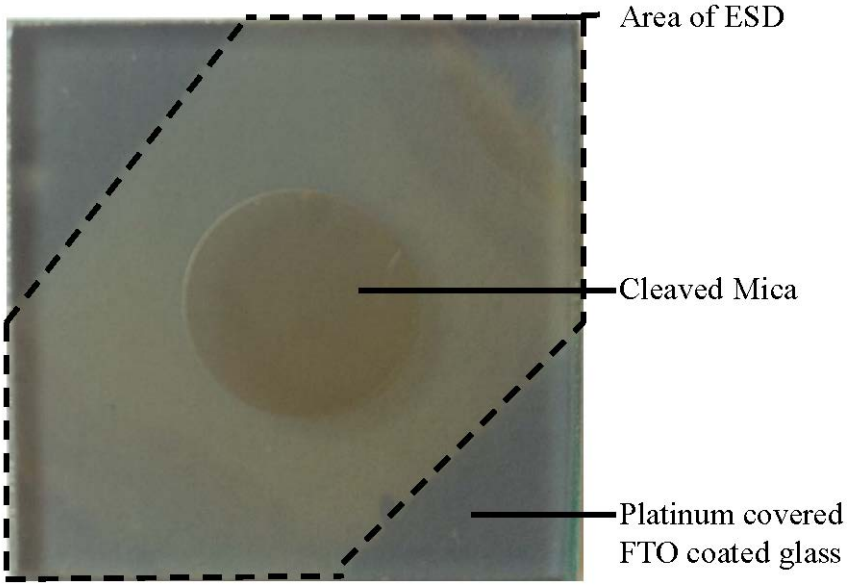

Figure 23. Image of a substrate after ESD. The center circle is the cleaved mica adhered to the FTO coated glass. A 2.7 nm layer of platinum was sputtered onto the mica and

glass. The top left and bottom right corners are free of PTEBS as they were conductively taped to the grounded aluminum plate of the electrospray apparatus.

Figure 25 is an AFM image showing the topology of a mica substrate covered with PTEBS particles after 1.5 minutes of ESD. The observed particle diameter ranges from 25 – 312 nm. The particles appear to be slightly wet upon deposition as evidenced by the residual rings seen around the particles. The rings are believed to have been created when the solvent from the droplets evaporated. Figure 26 is an AFM image of the surface profile of PTEBS particles after 1.5 minutes. There were 4 particles higher than 50 nm with the highest peak being 65 nm, while the majority of the particles were shorter than 25 nm.

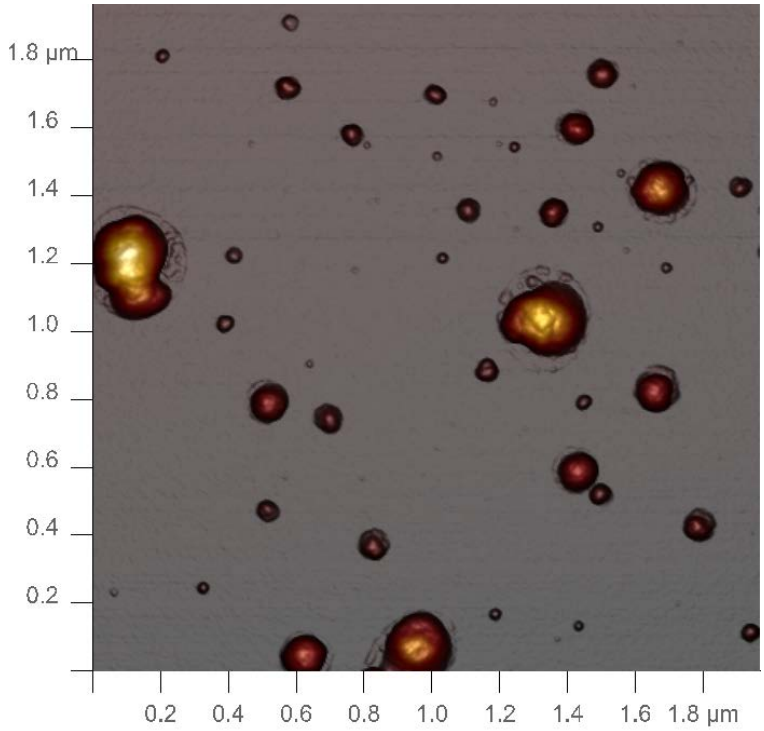

Figure 24. AFM topology of mica substrate covered with PTEBS particles after 1.5 minutes of ESD.

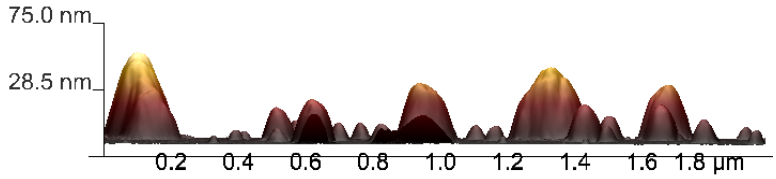

Figure 25. AFM profile image of PTEBS after 1.5 minutes of ESD.

Figure 27 is a histogram of the observed particle diameter from a 25 μm^2 section of mica after 3 minutes of ESD with PTEBS. Particle density was the only observed difference between 1.5 and 3 minutes of ESD. As can be seen, the majority of particles have diameters less than 52 nm and there are few particles in the size ranges above 77 nm.

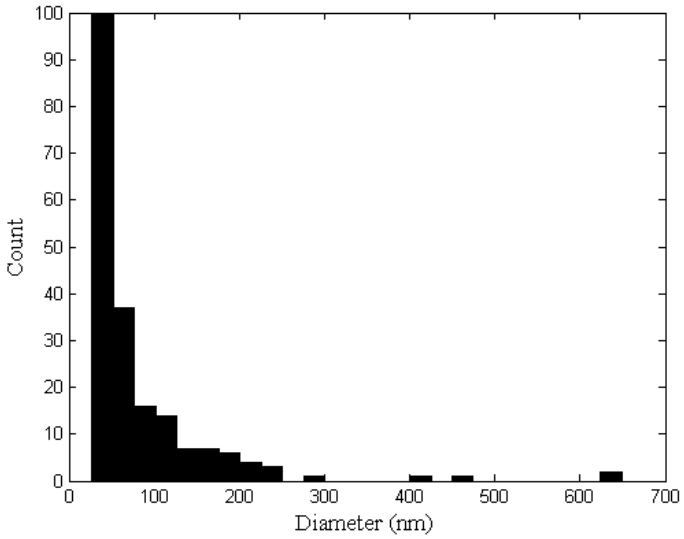

Figure 26. Particle diameter histogram of 25 μm^2 after ESD for 3 minutes.

Figure 28 is an AFM image showing the topology of a mica substrate covered with PTEBS particles after 5 minutes of ESD. The particles have begun to cluster around each other due to a fairly constant symmetrical spray plume. The particle deposition pattern is believed to be influenced by electrostatic forces. PTEBS is a weakly conducting polymer and only particles in close proximity to the grounded substrate are

discharged quickly. Deposited particles furthest away from the grounded substrate retain some charge and repel oncoming charged droplets toward a PTEBS-free region of the substrate. This explanation is referred to as ‘preferential landing’ and is supported by previous literature on ESD of thin films[81,102–104]. Deposited particles appear to have coalesced and merged together due to the presence of a small amount of solvent upon deposition. This is supported by the residual rings observed in Figure 25. Figure 29 is an AFM image of the surface profile of the PTEBS covered mica substrate after 5 minutes of ESD. The profile shows approximately 3 maximums above 50 nm with the majority of particles being less than 28.5 nm.

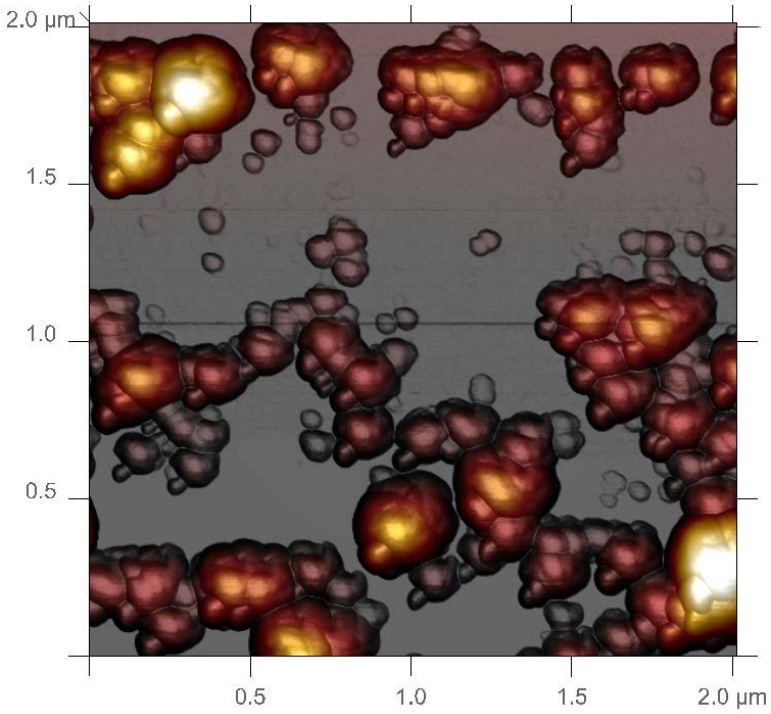

Figure 27. AFM topology of mica substrate covered with PTEBS particles after 5 minutes of ESD.

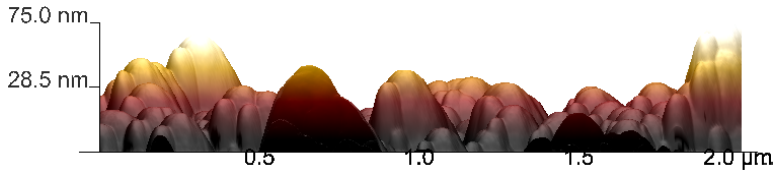

Figure 28. AFM profile image of PTEBS after 5 minutes of ESD.

Figure 30 is an image of the AFM topography of a mica substrate coated with a PTEBS thin film from ESD after 40 minutes. Due to the deposition of droplets, the particles coalesced and merged together to form a contiguous thin film. The RMS surface roughness was 20.2 nm and the film had an average thickness of 64.7 nm. Small valleys can be seen where the film expanded from larger particles due to preferential landing. Once the mica substrate was covered, smaller particles were no longer depositing on the thin film. Because the polymer film was poorly conducting, the small particles were electrostatically repelled by the previously deposited polymer (which still has a charge) and are attracted to the grounded FTO substrate and aluminum plate. Large particles continued to be deposited due to inertial forces dominating electrostatic forces resulting in large protrusions on the surface.

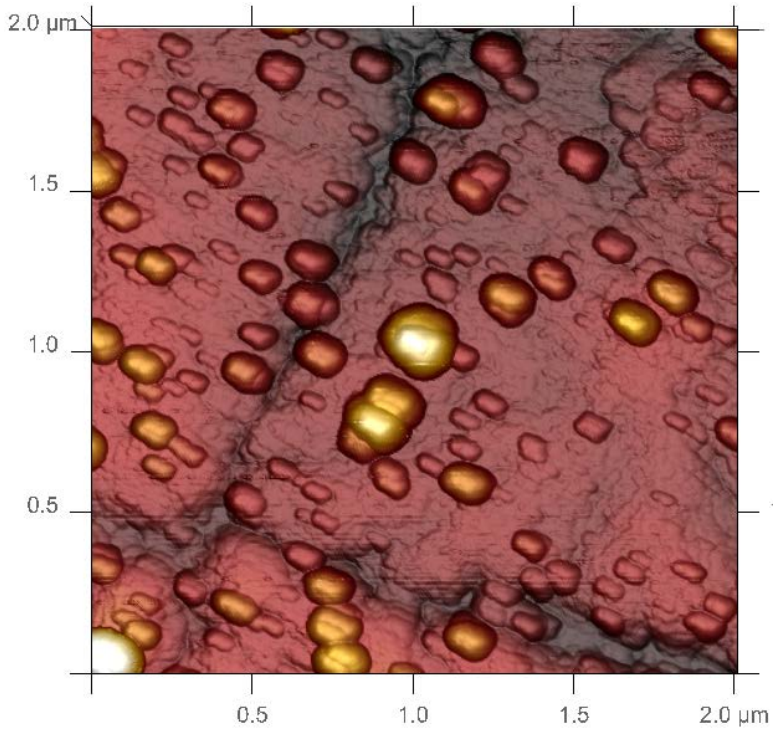

Figure 29. AFM topology of mica substrate covered with PTEBS thin film after 40 minutes of ESD.

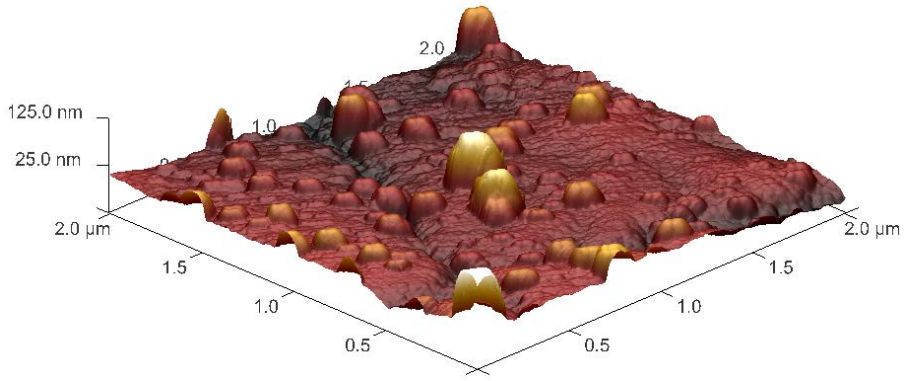

Figure 30. AFM angled image of PTEBS thin film after 40 minutes of ESD.

PTEBS thin films from ESD were characterized by a UV-Vis spectroscopy to ensure the PTEBS was not chemically altered through the ESD process and that the films maintained their absorption properties for use in PSCs. Figure 32 shows the absorption spectra of PTEBS films from ESD (600 nm and 1.2 µm) and drop casting (7 µm). The

absorption maximum occurred at wavelengths between 420 nm and 430 nm for all three films. These absorption maximums show no significant differences and correspond with previously reported values leading us to believe there was no chemical alteration by the ESD process [41,83,84]. The increased absorption shown in Figure 32 outside of the peak was caused by light scattering from the rough surface and internal grain boundaries within the ESD films [105,106].

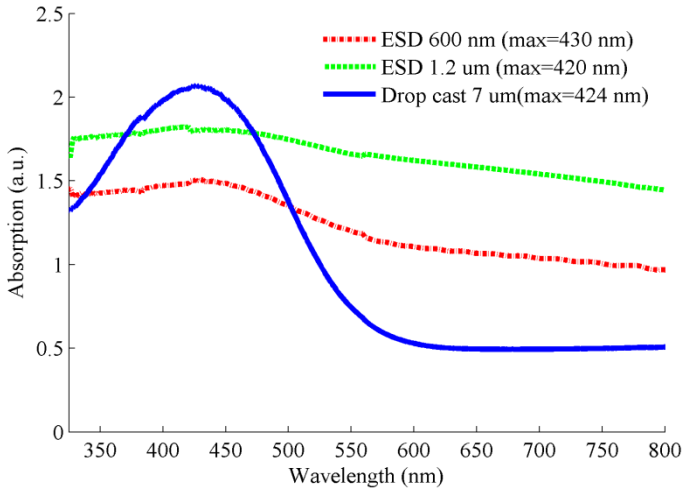

Figure 31. Absorption spectrum of PTEBS thin films from ESD (600 nm and 1.2 μm) and from drop casting (7 μm).

6. HYBRID SOLAR CELLS WITH TiO_2 NANOSTRUCTURES

Hybrid solar cells (HSC) consist of an inorganic semiconducting electron acceptor and an organic polymer electron donor sandwiched between a transparent conducting oxide anode and a metal cathode. They have attracted considerable attention due to low production cost, solution processing, and an array of different materials suitable for device fabrication [107–109]. HSCs take advantage of inorganic semiconductors' high electron mobilities ($TiO_2 \approx 0.001$ - 10 $cm^2V^{-1}s^{-1}$) [110,111] to overcome the poor hole mobilities in organic polymers (polythiophene polymers $\approx 0.00001 - 0.1$ $cm^2V^{-1}s^{-1}$) [112–115] which lead to short electron diffusion lengths (~10 nm) [116,117]. Therefore, the interface between the inorganic semiconductor and organic polymer in HSCs must be within one diffusion length of exciton generation to effectively separate excitons into holes and electrons. This presents a challenge to bilayer devices due to a limited interfacial contact area between the electron donor and acceptor layers. HSC devices have been designed with nanostructures (nanorods, nanoribbons, and inter-penetrating layers) to increase the interfacial surface area [36,38,118].

The polymers poly(3-hexylthiophene) [P3HT], poly(2-methoxy-5-(2-ethyl-hexyloxy)-p-phenylenevinylene) [MEH-PPV], and poly(3-octylthiophene) [P3OT] have widely been reported as electron donor materials in TiO_2 HSCs [94,119–121]. These polymers are soluble in organic solvents such as toluene, chloroform, chlorobenzene, tetrahydrofuran, and xylene which are toxic in nature [16]. Commercialization of polymer based solar cells will require generation of several gigwatts of power [44], which corresponds to a solar cell (~5% efficient) area of thousands of square meters [4]. The toxicity of organic solvents makes them a poor option on this order of magnitude due to

increased costs and difficulty of fabrication associated with environmental hazards. Water soluble polymers are an obvious alternative due to water's prevalence, low cost, and safety. The water soluble polymer PTEBS has been reported as an electron donor material in TiO_2 HSCs by Qiao et al. [40,41,84] and in polymer solar cells using fullerene derivatives [95,97].

In this work HSC devices were fabricated with a bi-layer structure of FTO/TiO_2/PTEBS/Au where ESD was compared to spin coating thin-films of the water-soluble polymer PTEBS above of an interpenetrating TiO_2 layer. Figure 33 shows an energy band diagram of the HSC devices fabricated, while Figure 34 depicts a device schematic. Light is absorbed by the PTEBS and an exciton is excited from the HOMO (-5.2 eV) to the LUMO (-3.2 eV) energy level [84]. The exciton is then separated into an electron and hole at the LUMO (-4.2 eV) of the TiO_2 is [118]. The electron travels to the fluorine-doped tin oxide (FTO) (-4.4 eV) electrode and the hole goes to the gold (-5 eV)electrode [122,123]. Average current densities were then modeled using the characteristic equation of an equivalent circuit of a solar cell.

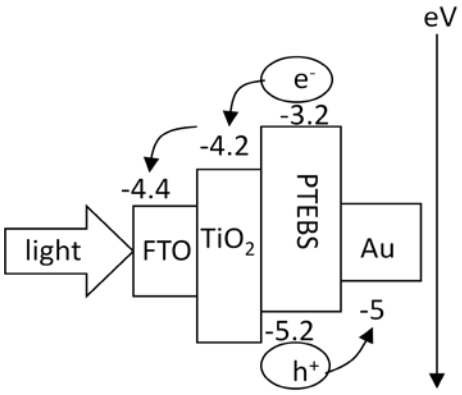

Figure 32. Energy band diagram for FTO/TiO2/PTEBS/Au devices. The band gap of PTEBS is ~2 eV. The estimated range of the LUMO is 2.7~-3.2 eV and the HOMO ranges from and -4.7~-5.2 eV [40]. The work functions of FTO, TiO_2, and gold are -4.4 eV [122], -4.2 eV [118], and -5 eV [123], respectively.

Figure 33. Schematic of bilayer heterojunction hybrid solar cell with configuration of glass/FTO/TiO_2/PTEBS/Au [40].

6.1 Experimental

Transparent conductive FTO coated glass substrates of 12.5 – 14.5 Ω sheet resistance were purchased from Hartford Glass Company. FTO substrates were then cleaned in ultrasonic baths of detergent, acetone, isopropanol, and water for 15 minutes each. Degussa P25 TiO_2 powder was suspended in 0.1 M acetic acid by sonication for 12 hours. The TiO_2 suspension was then left alone for 2 days to allow large particles to settle to the bottom before spin coating onto the FTO at 1700 rpm for 40 seconds to obtain a 2.1 μm thick layer. The TiO_2 was annealed for 1 hour at 500°C.

PTEBS was purchased from QCR solutions and dissolved in water at a 2% (by weight) concentration. The PTEBS layer was deposited by spin coating at 800 rpm to create a ~100 nm thick layer. Devices with a PTEBS layer from ESD were from a 0.5% solution in a water and ethanol blend with a 1:1 ratio before being loaded into a 1ml syringe with a 30 G hypodermic needle. The addition of ethanol was needed to lower the surface tension of the solution to maintain a steady Taylor cone for adequate film formation. Figure 21 illustrates a schematic of the electrospray configuration used to deposit PTEBS layers from ESD. The TiO_2 coated FTO substrate was adhered to an aluminum plate with copper tape. The distance between the needle tip and the grounded aluminum plate holding the FTO substrate was 7 cm. The flow rate through the needle,

controlled by a syringe pump, was 2 µl/min and the applied voltage was 7.5 – 9 kV. The ITO substrate was grounded to the aluminum plate and sprayed for 1 hour to create a ~100 nm thick layer. The 80 nm thick gold electrodes were then deposited via sputter coating through a mask to create 0.06 cm^2 devices.

6.2 Modeling of Equivalent Circuit

A single diode electrical equivalent circuit (Figure 35) of a solar cell was used as a model to compute output current densities (J_{out}). The equation describing the current-voltage characteristics of a solar cell is represented by Equation 1**.**

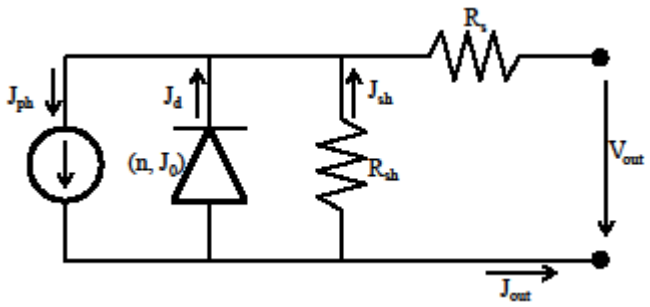

Figure 34. Equivalent circuit of a solar cell.

$$J_{out} = -J_0\left[exp\left(\frac{V_{out} + R_s J_{out}}{nV_{th}}\right) - 1\right] - \frac{V_{out} + R_s J_{out}}{R_{sh}} + J_{ph}$$

Equation 1. Current-Voltage characteristic equation of a solar cell.

Where J_{out} is the output current density, J_0 is the saturation current, V_{out} is the output voltage, R_s is the series resistance, n is the diode ideality factor, $V_{th} = \frac{kT}{q}$ is the thermal voltage (k is the Boltzmann constant, T is the temperature, and q is the elementary charge), R_{sh} is the shunt resistance, and J_{ph} is the photocurrent.

Equation **1** is a transcendental equation that expresses the current density output J_{out} as a function of itself and V_{out}. An explicit exact solution for Equation 1 can be

computed using the Lambert W function [124,125]. Equation 1 must be expressed in the form of $\omega e^{\omega} = x$ to utilize the Lambert W function where:

$$\omega = -\frac{R_s J_{out} + V_{out}}{nV_{th}} + \frac{R_s(J_0 + J_{ph}) + V_{out}}{nV_{th}(1 + G_p R_s)}$$

and

$$x = \frac{R_s J_0}{nV_{th}(1 + G_p R_s)} exp\left(\frac{R_s(J_0 + J_{ph}) + V_{out}}{nV_{th}(1 + G_p R_s)}\right)$$

where $G_p = 1/R_{sh}$. The solution to $\omega e^{\omega} = x$ is the function *Lambert* $W_k(x)$ where the branch (k) of the solution corresponds to k = 0 which satisfies *Lambert* $W_0(x) = 0$. For simplification *Lambert* $W = W$, the explicit solution of

Equation **1** becomes [124,125]:

$$J_{out} = -\frac{nV_{th}}{R_s} W\left[\frac{R_s J_0}{nV_{th}(1 + G_p R_s)} exp\left(\frac{R_s(J_0 + J_{ph}) + V_{out}}{nV_{th}(1 + G_p R_s)}\right)\right] - \frac{V_{out}}{R_s} + \frac{R_s(J_0 + J_{ph}) + V_{out}}{nV_{th}(1 + G_p R_s)}$$

Equation 2. Exact analytic solution of the current-voltage characteristic equation of a solar cell.

6.3 Results and Discussion

Table 2 displays the minimum, maximum, and average values of the short circuit current (J_{sc}), open circuit voltage (V_{oc}), and efficiency (η) of 15 different HSC with PTEBS layers from ESD and spin coating. Figure 36 is a current density (J) – voltage (V) plot of the average current density values of all devices for each construction type. The average J_{sc} for ESD devices was 0.0443 mA/cm^2 which was double the average J_{sc} of 0.0220 mA/cm^2 for spin coated devices. The average V_{oc} for ESD devices was 0.3406 V which was nearly half the average V_{oc} of 0.6493 V for spin coated devices. The average efficiency for ESD devices was 0.006%, slightly lower than the spin coated device

efficiency of 0.0076%. The maximum efficiencies achieved from both device constructions were comparable at 0.009%. The average standard deviation of the current densities was 0.0040 mA/cm^2 for the spin coated device construction and 0.0085 mA/cm^2 for the ESD device construction. ESD constructed devices have greater variations in morphology of the PTEBS layer which led to higher standard deviations and greater performance variation.

Table 2. Table of minimum, maximum, and average values of short circuit current (J_{sc}), open circuit voltage (V_{oc}), and efficiency (η) of 15 different HSC with electron donor layers from ESD and spin coating.

	Minimum			**Average**			**Maximum**		
	J_{sc} (mA/cm^2)	V_{oc} (V)	η (%)	J_{sc} (mA/cm^2)	V_{oc} (V)	η (%)	J_{sc} (mA/cm^2)	V_{oc} (V)	η (%)
ESD	0.0352	0.3400	0.0035	0.0443	0.3406	0.0060	0.0532	0.4200	0.0086
Spin	0.0186	0.5800	0.0060	0.0220	0.6493	0.0076	0.0245	0.7000	0.0088

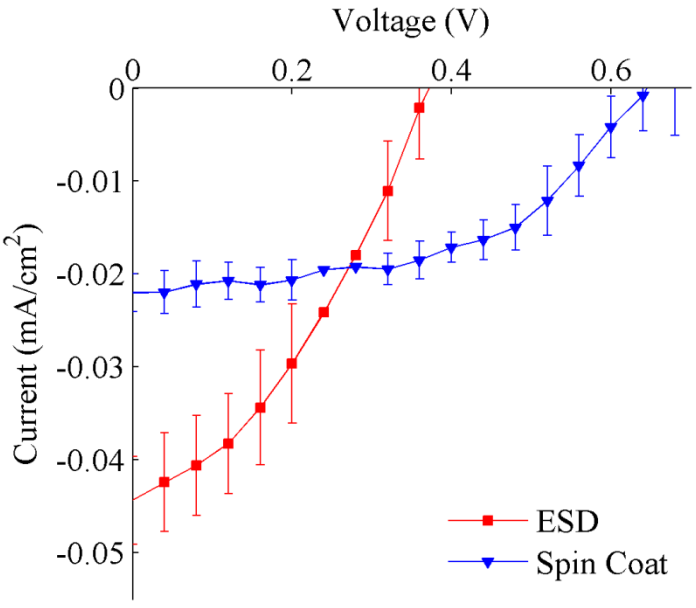

Figure 35. Average $J - V$ curves of 15 different devices from each deposition method of the PTEBS layer. The error bars show the standard deviation of the current along each

measured voltage value. Error bars were omitted from points at the intersection for clarity.

The substantial differences in J_{sc} and V_{oc} between the two different device constructions are likely due to the differences in the interfacial contact area between the TiO_2 and the PTEBS, and the morphology of the PTEBS layer. Figure 37 is an SEM image of the TiO_2 inter-penetrating network of nanoparticles. The average pore size is ~50 nm with a range of 10 – 100 nm.

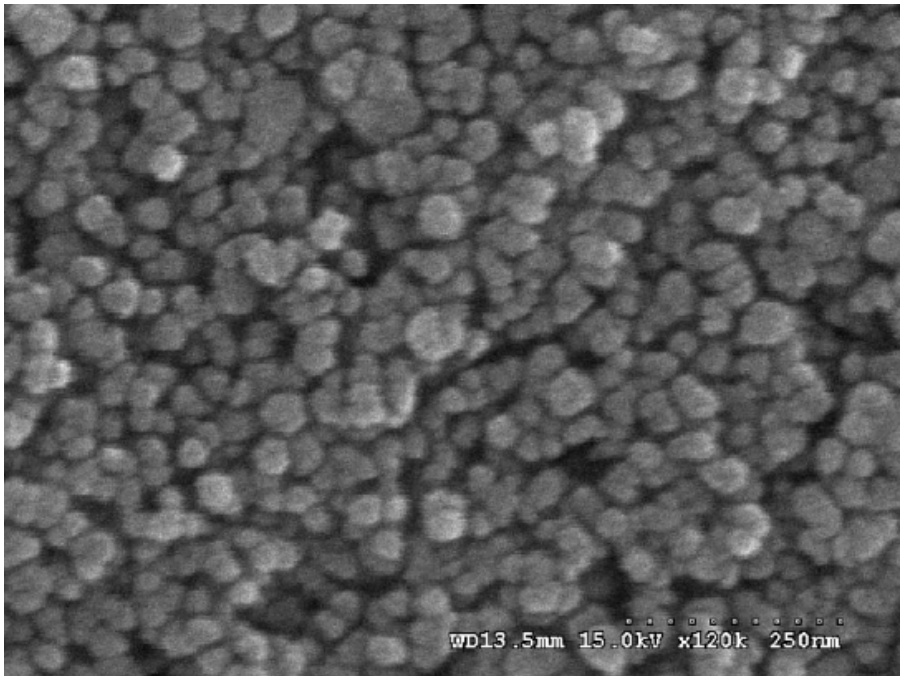

Figure 36. SEM image of the inter-penetrating nanocrystalline TiO_2 film at 120,000x magnification.

When using the spin coating technique, the surface tension of the water inhibits the PTEBS solution from filling the nano-pores of the TiO_2 layer. Poor filling of porous TiO_2 nanostructures has been extensively reported as a deficiency in HSC [111,112,126–129]. By contrast, the ESD technique can lead to improved pore filling for two reasons. First, ESD generates particles small enough to penetrate the pores in the TiO_2 film. A histogram of particle diameters from ESD (Figure 27) reveals that the majority of PTEBS

particles upon deposition are in the first bin, which ranges between 20 – 51.9 nm and has a median of 39.5 nm. The particles are able to penetrate the pores of the TiO_2 film and increase the interfacial contact area between the TiO_2 and PTEBS layers. In addition, the particles generated by ESD are electrically charged and are driven by the applied electric field. The electrostatic force also helps push the particles into the nano-pores leading improved interfacial contact area.

The ESD film suffers from interfacial boundaries from individual PTEBS particles that did not fully coalesce upon deposition. Kim et al. reported that these boundaries diminish the performance of polymer solar cells [77]. Figure 38 is an AFM image of a PTEBS film from ESD showing that the film surface has some interfacial boundaries between particles even though it is a contiguous film. Film irregularities are believed to be the reason for a decrease in V_{oc}. The ESD film had a root mean squared surface roughness of 20.2 nm. The uniformity of a spin coated film as compared to an ESD film is a likely source for an increased standard deviation of output current density in devices with ESD construction.

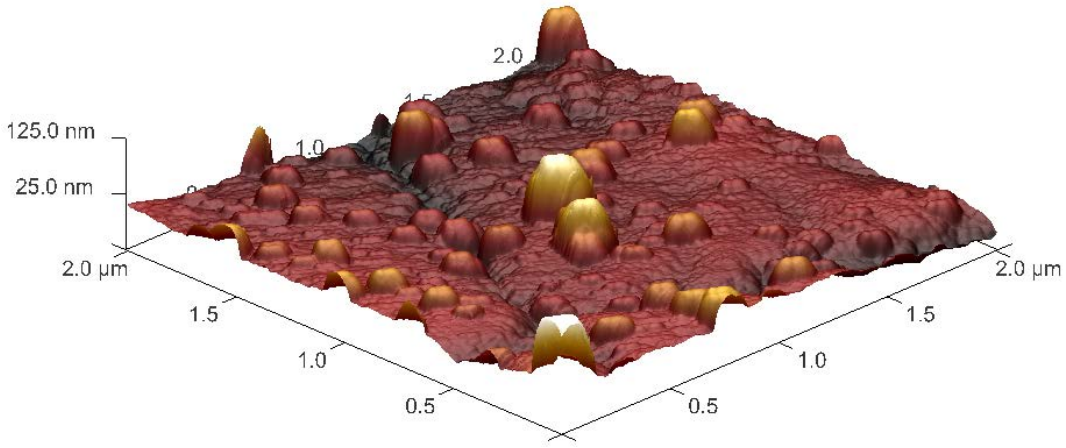

Figure 37. AFM image of PTEBS film from ESD.

The average $J - V$ curves from both construction techniques were then modeled using the characteristic equation of solar cells (Equation 1). Figure 39 shows the model curves along with the average illuminated $J - V$ curves. The following parameter values used in the model were kept constant and agree with previously reported values [130–132]: $R_s = 4.2\ \Omega$, $R_{sh} = 100\ \Omega$, n = 2.14, k = 1.38×10^{-23} J/K, q = 1.6×10^{-19} C, and T = 300 K. The values of the series and shunt resistance were chosen because they gave the curves the proper shape. The reverse saturation current density (J_0) and the photocurrent density (J_{ph}) were the used to fit the experimental curves. . The spin coated $J - V$ curve agreed with the model at values of $J_{ph} = 0.047$ mA/cm^2 and $J_0 = 3.72 \times 10^{-5}$ mA/cm^2, and the ESD J – V curve agreed to the model with values of $J_{ph} = 0.023$ mA/cm^2 and $J_0 = 2.2 \times 10^{-7}$ mA/cm^2. Increases in J_{ph} due to an increase in the interfacial contact area between the polymer and TiO_2 were also reported by Tanaka [133]. Our model shows that devices with PTEBS films from ESD generate double the amount of J_{ph}, and an increase of two orders of magnitude in the J_0 compared to devices constructed from spin coating. The increase in J_0 is attributed to poor film quality of ESD PTEBS films. The interfacial boundaries between PTEBS particles increase leakage current through the device sidewalls similar to decreasing R_{sh}, which is known to decrease V_{oc} [77,124,125,134,135]. Our model responds better by varying J_0 rather than R_{sh} to demonstrate the effect of poor film quality on V_{oc}.

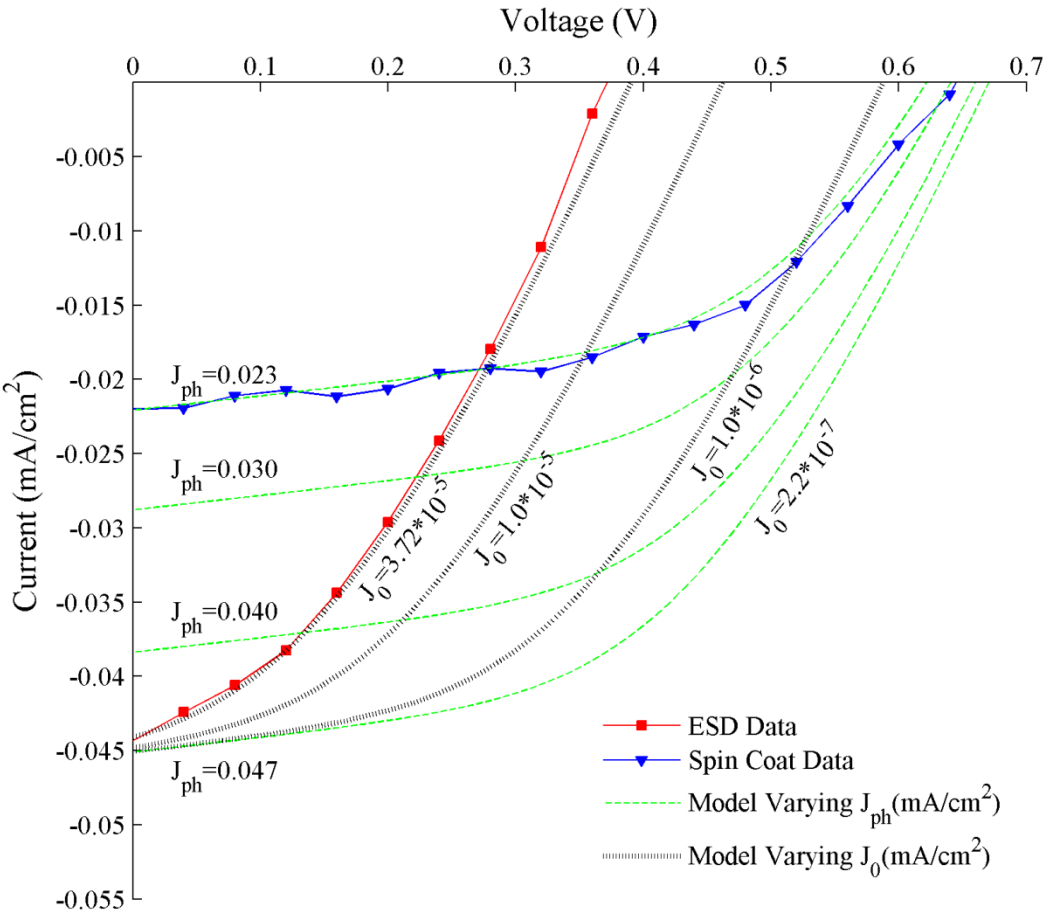

Figure 38. Illuminated average $J - V$ curves from experimental data and computational models. Model lines varying J_{ph} held a constant $J_0 = 2.2 \times 10^{-7}$ mA/cm^2. Model lines varying J_o held a constant $J_{ph} = 0.047$ mA/cm^2.

Figure 40 shows the dark $J - V$ curves of typical devices of each construction type along with the model curves. The J_0 values in the model curves were the best fits (J_{0spin} = 3.72x10^{-5} mA/cm^2 and $J_{0ESD} = J_0$ = 2.2x10^{-7} mA/cm^2) from the illuminated $J - V$ curves and J_{ph} = 0 mA/cm^2. The ESD model agrees very well with the experimental data while the spin coated model deviates slightly at higher voltages. However, but the trend of the curvature is largely in agreement.

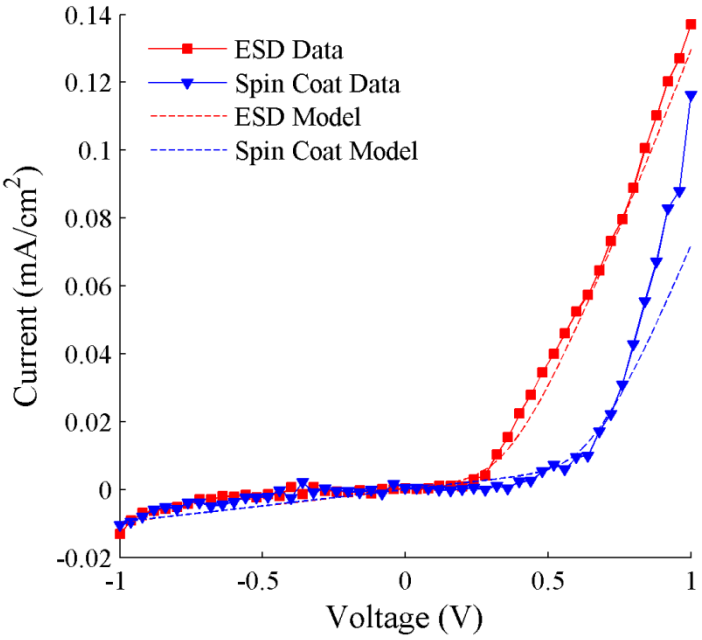

Figure 39. Dark *J* – *V* curves of experimental data and model.

7. POLYMER SOLAR CELLS WITH FULLY WATER SOLUBLE ACTIVE LAYERS BY ELECTROSPRAY DEPOSITION

The structure of a polymer solar cell (PSC) (and hence efficiency) is intimately linked to the processing conditions during fabrication, and commercialization of PSCs will require reliable and scalable fabrication processes. Traditional laboratory-scale PSC devices are commonly prepared by a two step solution process where two different layers are spin casted consecutively. The first layer typically being a dispersion of poly(3,4-ethylene dioxythiophene)-poly(styrene sulfonate) (PEDOT:PSS) in water [136], and the second being a bulk heterojunction active layer dissolved in an organic solvent [107]. However, spin casting is a low throughput and high waste process where much of the polymer is lost due to the high rotational speeds. A second problem with the traditional laboratory fabrication method is the inability for consecutive layering from common solvents. In order to add multiple layers of polymer, a solvent orthogonal to the previous layer is needed to prevent dissolution. Another potential disadvantage associated with the spin casting of a bulk solution is the presence of a vertical phase gradient due to the penetration of less soluble components [137,138]. These obstacles hinder simple, low-cost, commercially favorable solution based processes.

Electrospray deposition (ESD) is a method of depositing thin films which can overcome the problems associated with spin coating. First, ESD is inexpensive, efficient (minimal waste), and has a relatively high throughput [45] making it practical for large scale commercialization. Second, it overcomes the solubility issue between two adjacent layers. ESD generates nebulized aerosol particles which, depending on solvent volatility, can be nearly dry upon deposition so that prior layers do not dissolve. Recently, there

have been reports of successful fabrication of PSCs consisting of P3HT and PCBM electrosprayed from organic solvents onto a spin casted layer of PEDOT:PSS [77,78,139]. ESD can also be advantageous for controlled vertical (uniform and gradient) deposition of thin-films.

Another major issue in the commercialization of PSCs is the toxic nature of organic solvents typically used in the deposition process. Organic solvent exposure can be toxic to the nervous system, and can lead to reproductive damage, liver and kidney damage, respiratory impairment, cancer, and dermatitis [16]. Large scale application of PSC relies on fabrication volumes generating several gigawatts of power [44], which corresponds to a PSC (~5% efficient) area of thousands of square meters [4]. Organic solvents are a poor option on this order of magnitude rendering environmentally friendly alternatives imperative. Environmentally friendly working conditions would significantly reduce ease and cost of commercializing PSCs.

Water is an obvious alternative solvent due to its prevalence and safety, however low efficiencies (<1%) of devices fabricated from water soluble polymers have prevented it from being widely investigated as a viable solvent for PSC. Q. Qiao and J.T. McLeskey were the first to fabricate a PSC from a water-soluble polymer, sodium poly[2-(3-thienyl)-ethyloxy-4-butylsulfonate] (PTEBS), in 2005. They reported an efficiency of 0.13% from a device structure of FTO/TiO2/PTEBS/Au [40]. A.J. Miller et al. has reported the highest efficiency (0.56%) PSC device from a water-soluble polymer (PTEBS) [97]. In 2011, Sondergaard et al. reported a PSC from all water processing with an efficiency of 0.7%, the highest known from water. They modified poly-3-

carboxydithiophene (P3CT) and PCBM into analogues for aqueous processing, through neither are truly water-soluble [44].

In this work ESD was utilized to create bulk heterojunction (BHJ) thin-films of the water-soluble polymer PTEBS (Figure 16) and the fullerene derivative C_{60} pyrrolidine tris-acid (Figure 18) for use in polymer solar cells. Water solubility combined with ESD enables fabrication of PSCs in environmentally friendly conditions with low cost and high throughput, a combination that is necessary for commercialization. ESD enables consecutive deposition of two water soluble layers on top of one another; the hole conducting PEDOT:PSS layer and the BHJ layer of the water soluble polymer and fullerene derivative. Figure 41 shows an energy band diagram of the ITO/PEDOT:PSS/bulk(PTEBS+C_{60})/Al PSC device configuration. The ratio of PTEBS to C_{60} pyrrolidine tris-acid was varied from 1:1 to 1:3.

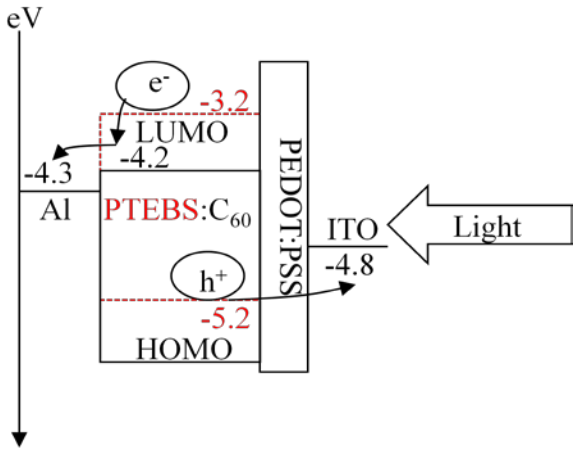

Figure 40. Energy band diagram of PSC with bulk heterojunction active layer comprised of water soluble materials, PTEBS and C_{60} derivative.

PTEBS was chosen to be the electron donor of the active layer due to the numerous reports of successful PSC devices [40–42,84,94,96,97,140]. The HOMO and LUMO

energy levels of PTEBS are -5.2 and -3.2 [84]. The LUMO of C_{60} tris-acid is estimated to be -4.2 eV using values from similar water-soluble fullerenes reported in the literature [85–88].

7.1 Experimental

Transparent conductive ITO coated glass substrates of 8 – 12 Ω sheet resistance were purchased from Sigma Aldrich. ITO was then etched completely from the edge of the glass using HCl to form a patterned bottom electrode for testing purposes before being sonicated in detergent, acetone, isopropanol, and water for 15 minutes each. PEDOT:PSS (Clevios P VP Al 4083) was then spin coated at 5000 rpm for 40 seconds and annealed at 100°C for 1.5 hours.

The water-soluble polythiophene PTEBS was purchased from QCR Solutions. The water-soluble C_{60} pyrrolidine tris-acid was purchased from Sigma Aldrich. Separate stock solutions of PTEBS and C_{60} were created by dissolving in DI water at a concentration of 2% by weight. Solutions were stirred for three days at room temperature. Stock solutions were then combined to form a bulk solution. Water and ethanol were added to dilute the bulk solution to 0.5% with a solvent ratio of 1:1. The bulk solution was then sonicated for 15 minutes immediately before being loaded into a 1 ml syringe with a 30 gauge hypodermic needle.

Figure 21 illustrates a schematic of the electrospray configuration used to deposit the bulk heterojunction active layer. The distance between the needle tip and the grounded aluminum plate was 7 cm. The flow rate through the needle, controlled by a syringe pump, was 2 μl/min and the applied voltage was 7.5 – 9 kV. The ITO substrate was grounded to the aluminum plate and sprayed for 1.5 hours. The 100 nm thick

aluminum electrodes were then deposited via electron beam evaporation (at 10^{-6} Torr) through a mask to create six different 0.115 cm^2 devices.

Device characterization was performed under 100 mW/cm^2 illumination using 1.5 AM light from a Spectra-Physics 96000 150 W Solar Simulator. Current and voltage source/measurements were obtained using a Keithley 236.

7.2 Results and Discussion

The current density - voltage curves of the PSCs are shown in Figure 42. Active layers with ratios of PTEBS to C_{60} tris-acid of 1:1, 1:2, and 1:3 all created working devices. The highest power conversion efficiency observed was 0.0022% from the device with a 1:2 ratio. The efficiency of the 1:3 ratio device was 0.0021% while the 1:1 ratio device performed at 0.00098%. The short circuit current density (J_{sc}) increased from 0.0069 mA/cm^2 to 0.0164 mA/cm^2 and then to 0.0241 mA/cm^2 as the amount of C_{60} tris-acid increased. The presence of C_{60} tris-acid molecules is directly related to electron mobility and improved device currents as its percentage increased. The open circuit voltage (V_{oc}) increased from 0.48 V in the 1:1 ratio device to 0.56 V in the 1:2 ratio device. The V_{oc} then decreased to 0.40 V in the 1:3 ratio device making it have the lowest V_{oc} while achieving the highest J_{sc}. Based on these results we conclude that the optimal ratio is between 1 part PTEBS and between 2 and 3 parts C_{60} tris-acid by weight.

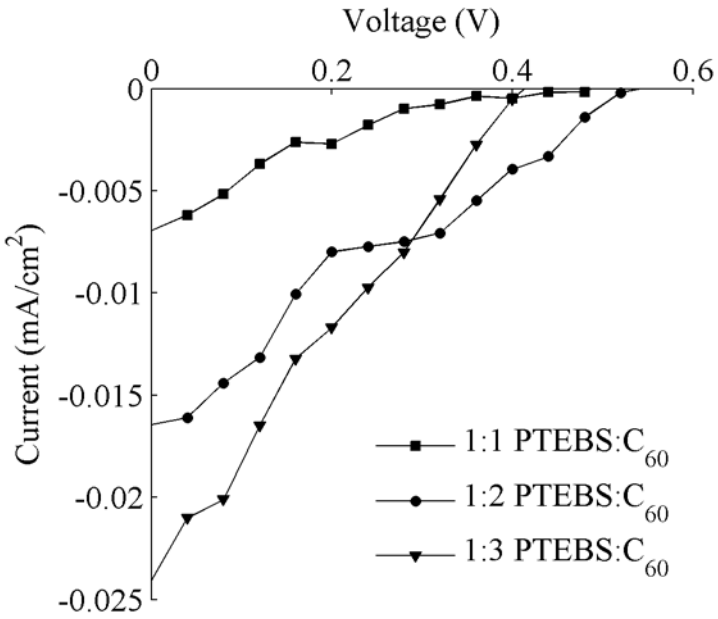

Figure 41. J-V Curves of PSC with Water-Soluble Active Layers from ESD. The ratio of the polymer PTEBS to C_{60} tris-acid is varied from 1:1 to 1:3.

The fill factor for the 1:2 ratio device was the highest at 0.25, while the 1:1 and 1:3 ratio devices were 0.16 and 0.23, respectively. Devices with higher fill factors extract more electrical power from a more constant current over a higher voltage as seen in the 1:2 ratio device.

Interestingly, these polymer-based devices exhibited excellent thermal stability. Initial current-voltage measurements were taken immediately after removal from vacuum (aluminum electrode deposition). Devices were then annealed at 150°C for 1 hour, cooled to room temperature, and then measured again. Resulting current-voltage measurements were nearly identical to initial measurements.

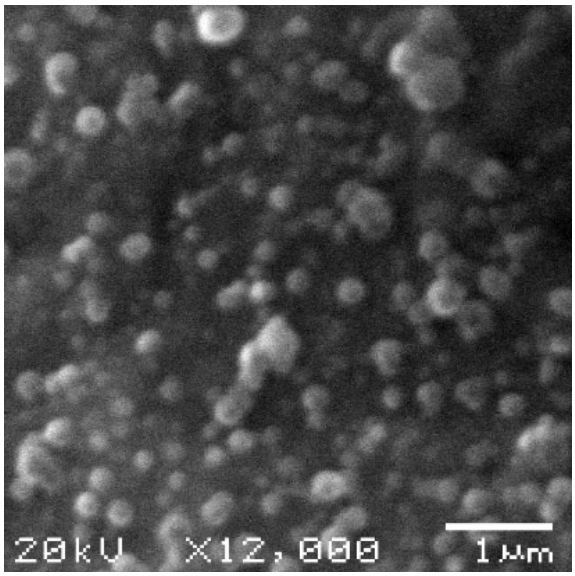

Figure 42. SEM image of aluminum electrode above an active layer from ESD.

The thickness of the PEDOT:PSS and active layer combined ranged between 200 and 350 nm as measured by an Ambios XP-1 profilometer. The thickness of the PEDOT:PSS layer was immeasurable due to it being thinner than the surface roughness of the ITO layer, but is expected to be less than 50 nm. Figure 43 shows a typical SEM image of a device at x12,000 magnification. The surface was not smooth and the ESD produced films consisting of relatively uniform sub-micron particles. The average particle appears to be less than 500 nm in diameter and consists of the PTEBS:C_{60} active layer coated with a 100 nm aluminum electrode layer, . These sub-micron particles of a polymer-C_{60} blend offer promise for the development of a new class of devices based on nanoparticles where the small diameter of the particle will allow for improved hole collection.

The optimal balance between PTEBS and C_{60} occurred between 1 part PTEBS and 2 to 3 parts C_{60}. This is believed to be where the percolation threshold of C_{60} occurs. Figure 44 illustrates the three different active layer ratios studied. In the 1:1 ratio there is

an insufficient amount of C_{60} to harvest the excitons from the PTEBS and transfer the electrons to the aluminum electrode. The excitons generated near the aluminum electrode are likely the only source of photocurrent, whereas excitons generated throughout the rest of the active layer may not be in close proximity to a C_{60} molecular chain that is in contact with the aluminum electrode. Excitons that undergo charge separation at a C_{60} interface that does not extend to the aluminum electrode are likely to recombine due to poor carrier mobility in the polymer. In the 1:2 and 1:3 ratio devices, the percolation threshold of C_{60} was achieved demonstrated by the increase in J_{sc}. The 1:3 ratio device had insufficient photon absorption due to a deficiency of PTEBS, leading to a reduced V_{oc}.

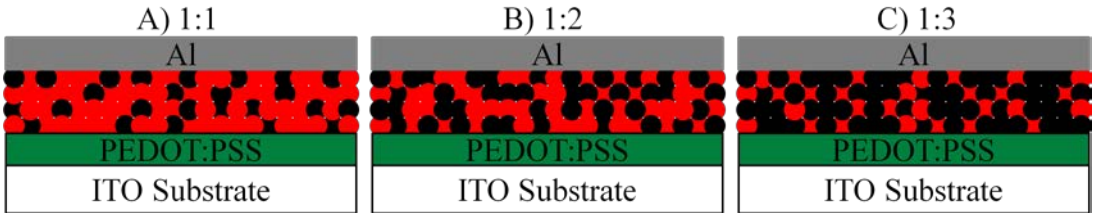

Figure 43. Illustration of active layers with varying PTEBS:C_{60} ratios. Percolation threshold of C_{60} was achieved in devices B and C, where C_{60} molecular chains extend randomly throughout the active layer.

8. CONCLUSIONS

We have demonstrated the ability of ESD to fabricate water soluble polymer (PTEBS) thin films of less than 100 nm for use in organic polymer solar cells, light emitting diodes, and SAW sensors. Maintaining a steady Taylor cone and slightly wet particle deposition were the most critical aspects in fabricating thin films from ESD which was achieved by adjusting the following parameters: distance between spray tip and grounded substrate, flow rate through the needle, applied voltage, and solution properties. The Taylor cone formed at the tip of the hypodermic needle and generated a majority of droplets less than 52 nm in diameter. Particles were deposited slightly wet which enabled coalescing with previously deposited particles which have dried to form a contiguous thin film. Electrostatic forces from deposited particles at thicker film areas repulsed smaller oncoming particles towards bare areas of the grounded substrate until a film covered the entire substrate. A contiguous thin film was obtained after 40 minutes of ESD with a thickness of 64.7 nm and an RMS roughness of 20.2 nm. UV-Vis measurements showed consistent absorption maximums indicating no alteration of PTEBS chemical structure from ESD. Efforts are underway to incorporate PTEBS thin films in polymer solar cells.

We conclude that ESD of water soluble polymer PTEBS thin films results in comparable efficiencies to traditional spin coating of thin films in TiO_2 solar cells. Device constructions from ESD generate nearly double the J_{sc} but approximately half the V_{oc} as spin coated films. Devices from ESD have a larger standard deviation in current density due to greater variations in film morphology. The increase in J_{sc} is attributed to a greater interfacial contact area between the PTEBS and TiO_2 layers due to the superior

penetration of electrosprayed PTEBS droplets into the pores of the TiO_2. Surface tension of the water prevents adequate penetration of the TiO_2's pores during spin coating. Poor film quality and surface roughness from interfacial boundaries between particles in the PTEBS layers from ESD are responsible for decreased *Voc*. An exact analytic solution using the Lambert W function was used to model the experimental data from both devices construction types. The model showed an increase by a factor of 2 in J_{ph} in the ESD construction and an increase in J_0 of two orders of magnitude in the ESD construction. The model also agreed with dark $J - V$ curves when $J_{ph} = 0$ mA/cm^2.

We have fabricated polymer solar cells with fully water-soluble active layers by electrospray deposition. The devices show modest photovoltaic response but show promise for the incorporation of water-soluble polymers and large-scale commercialization via electrospray deposition. A single device structure of ITO/PEDOT:PSS/bulk(PTEBS+C_{60})/Al was used to study the effect of PTEBS to C_{60} tris-acid ratio on photovoltaic performance. An active layer ratio of PTEBS:C_{60} tris-acid (1:2) achieved the highest power conversion efficiency (0.0022%), fill factor (0.25), and open circuit voltage (0.56 V). The percolation threshold of C_{60} was achieved between 1 part PTEBS and 2 to 3 parts C_{60}. Increasing the C_{60} tris-acid ratio (1:3) improved short circuit current, but reduced the open circuit voltage enough to lower efficiency. The incorporation of other water-soluble C_{60} derivatives is expected to enhance the efficiency and will be the subject of future study.

REFERENCES

[1] IEA, 2012 Key World Energy Statistics, Paris, France, 2012.

[2] M. Hubbert, Darcy's law and the field equations of the flow of underground fluids, Hydrological Sciences Journal. 2 (1957) 23–59.

[3] J.A. Duffie, W.A. Beckman, Solar Energy Thermal Processes, 1st ed., John Wiley & Sons, Inc, 1974.

[4] N.S. Lewis, D.G. Nocera, Powering the planet: chemical challenges in solar energy utilization., Proceedings of the National Academy of Sciences of the United States of America. 103 (2006) 15729–35.

[5] S. Günes, H. Neugebauer, N.S. Sariciftci, Conjugated polymer-based organic solar cells., Chemical Reviews. 107 (2007) 1324–38.

[6] M. Green, K. Emery, Solar cell efficiency tables (version 39), Progress in …. (2012) 12–20.

[7] R. Service, Outlook Brightens for Plastic Solar Cells, Science. 332 (2011) 293.

[8] C. Deibel, V. Dyakonov, Polymer–fullerene bulk heterojunction solar cells, Reports on Progress in Physics. 73 (2010) 096401.

[9] W. Shockley, H.J. Queisser, Detailed Balance Limit of Efficiency of p-n Junction Solar Cells, Journal of Applied Physics. 32 (1961) 510.

[10] G. Dennler, M.C. Scharber, C.J. Brabec, Polymer-Fullerene Bulk-Heterojunction Solar Cells, Advanced Materials. 21 (2009) 1323–1338.

[11] J. Kalowekamo, E. Baker, Estimating the manufacturing cost of purely organic solar cells, Solar Energy. 83 (2009) 1224–1231.

[12] EIA, Annual Energy Outlook 2012, 2012.

[13] A. Slaoui, R. Collins, Advanced inorganic materials for photovoltaics, Mrs Bulletin. 32 (2007) 211–218.

[14] L. Kazmerski, Solar Cell Efficiency Plot of Various Photovoltaic Technologies 1976-2011, (2011).

[15] M. Jørgensen, K. Norrman, F.C. Krebs, Stability/degradation of polymer solar cells, Solar Energy Materials and Solar Cells. 92 (2008) 686–714.

[16] U.S. Department of Labor, Solvents - Safety and Health Topics-OSHA, (2007).

[17] J. Roncali, Conjugated poly (thiophenes): synthesis, functionalization, and applications, Chemical Reviews. (1992) 711 – 738.

[18] S.-S. Sun, N.S. Sariciftci, Organic Photovoltaics: Mechanisms, Materials, and Devices, CRC Press, Boca Raton, FL, 2005.

[19] D.M. Chapin, C.S. Fuller, G.L. Pearson, A New Silicon p-n Junction Photocell for Converting Solar Radiation into Electrical Power, Journal of Applied Physics. 25 (1954) 676.

[20] M.A. Green, K. Emery, Y. Hishikawa, W. Warta, E.D. Dunlop, Solar cell efficiency tables (version 39), (2012) 12–20.

[21] A.L. Fahrenbruch, R.H. Bube, Fundamentals of Solar Cells, Academic Press, Inc., New York, 1983.

[22] D.E. Carlson, C.R. Wronski, Amorphous silicon solar cell, Applied Physics Letters. 28 (1976) 671.

[23] S. Guha, J. Yang, A. Banerjee, Amorphous silicon alloy photovoltaic research—present and future, … in Photovoltaics: Research and …. 150 (2000) 141–150.

[24] J. Yang, a. Banerjee, S. Guha, Triple-junction amorphous silicon alloy solar cell with 14.6% initial and 13.0% stable conversion efficiencies, Applied Physics Letters. 70 (1997) 2975.
[25] A.K. Ghosh, Rectification, space-charge-limited current, photovoltaic and photoconductive properties of Al/tetracene/Au sandwich cell, Journal of Applied Physics. 44 (1973) 2781.
[26] C. Chiang, C.F. Jr, Y. Park, Electrical conductivity in doped polyacetylene, Physical Review Letters. 39 (1977) 1098–1101.
[27] C.W. Tang, Two-layer organic photovoltaic cell, Applied Physics Letters. 48 (1986) 183.
[28] Y. Harima, K. Yamashita, H. Suzuki, Spectral sensitization in an organic p-n junction photovoltaic cell, Applied Physics Letters. 45 (1984) 1144.
[29] N. Sariciftci, D. Braun, C. Zhang, Semiconducting polymers and buckminsterfullerene heterojunctions: Diodes, photodiodes, and photovoltaic cells, Applied Physics …. (1993).
[30] M.T. Dang, L. Hirsch, G. Wantz, P3HT:PCBM, Best Seller in Polymer Photovoltaic Research, Advanced Materials. (2011) n/a–n/a.
[31] A. Mayer, S. Scully, B. Hardin, Polymer-based solar cells, Materials Today. 10 (2007) 28–33.
[32] M. Helgesen, R. Søndergaard, F.C. Krebs, Advanced materials and processes for polymer solar cell devices, Journal of Materials Chemistry. 20 (2010) 36.
[33] A.J. Moulé, J.B. Bonekamp, K. Meerholz, The effect of active layer thickness and composition on the performance of bulk-heterojunction solar cells, Journal of Applied Physics. 100 (2006) 094503.
[34] B.C.J. Brabec, C. Winder, N.S. Sariciftci, J.C. Hummelen, A. Dhanabalan, P.A. Van Hal, et al., A low-bandgap semiconducting polymer for photovoltaic devices and infrared emitting diodes, Advanced Functional …. (2002) 709–712.
[35] W.J.E. Beek, M.M. Wienk, R. a. J. Janssen, Hybrid Solar Cells from Regioregular Polythiophene and ZnO Nanoparticles, Advanced Functional Materials. 16 (2006) 1112–1116.
[36] A.M. Peiro, P. Ravirajan, K. Govender, D.S. Boyle, P. O'Brien, D.D.C. Bradley, et al., Hybrid polymer/metal oxide solar cells based on ZnO columnar structures, Journal of Materials Chemistry. 16 (2006) 2088.
[37] Y.-Y. Lin, C.-W. Chen, T.-H. Chu, W.-F. Su, C.-C. Lin, C.-H. Ku, et al., Nanostructured metal oxide/conjugated polymer hybrid solar cells by low temperature solution processes, Journal of Materials Chemistry. 17 (2007) 4571.
[38] D. Cheyns, K. Vasseur, C. Rolin, J. Genoe, J. Poortmans, P. Heremans, Nanoimprinted semiconducting polymer films with 50 nm features and their application to organic heterojunction solar cells., Nanotechnology. 19 (2008) 424016.
[39] K. Tvingstedt, V. Andersson, F. Zhang, O. Inganäs, Folded reflective tandem polymer solar cell doubles efficiency, Applied Physics Letters. 91 (2007) 123514.
[40] Q. Qiao, J.T. McLeskey, Water-soluble polythiophene/nanocrystalline TiO2 solar cells, Applied Physics Letters. 86 (2005) 153501.

[41] Q. Qiao, Y. Xie, J.T. McLeskey, Organic/Inorganic Polymer Solar Cells Using a Buffer Layer from All-Water-Solution Processing, Journal of Physical Chemistry C. 112 (2008) 9912–9916.
[42] J. Yang, A. Garcia, T.-Q. Nguyen, Organic solar cells from water-soluble poly(thiophene)/fullerene heterojunction, Applied Physics Letters. 90 (2007) 103514.
[43] W. Yu, H. Zhang, Z. Fan, J. Zhang, H. Wei, D. Zhou, et al., Efficient polymer/nanocrystal hybrid solar cells fabricated from aqueous materials, Energy & Environmental Science. 4 (2011) 2831.
[44] R. Søndergaard, M. Helgesen, M. Jørgensen, F.C. Krebs, Fabrication of Polymer Solar Cells Using Aqueous Processing for All Layers Including the Metal Back Electrode, Advanced Energy Materials. 1 (2011) 68–71.
[45] A. Jaworek, Electrospray Technology for Thin-Film Deposition, Nova Science Publishers, Inc., New York, 2010.
[46] W. Gilbert, De Magnete, Dover Publications, New York, 1600.
[47] a. Nollet, M. Watson, Extract of a Letter from the Abbe Nollet, F.R.S. &c. to Charles Duke of Richmond, F. R. S. Accompanying an Examination of Certain Phaenomena in Electricity, Published in Italy, by the Same, and Translated from the French by Mr. Watson, F. R. S., Philosophical Transactions of the Royal Society of London. 46 (1749) 368–397.
[48] Lord Rayleigh, On the Equilibrium of Liquid Conducting Masses Charged with Electricity, Philosophical Magazine. 14 (1882) 184–186.
[49] G. Alessandro, K. Tang, Charge and fission of droplets in electrostatic sprays, Physics of Fluids. 6 (1994).
[50] G. Taylor, Disintegration of water drops in an electric field, Proceddings of the Royal Society of London. Series A, Mathematical and Physical Sciences. 280 (1964) 383–397.
[51] J.B. Fenn, M. Mann, C.K. Meng, S.F. Wong, M. Craig, C.K.A.I. Meng, et al., Electrospray Ionization of Large for Mass Spectrometry Biomolecules, 246 (2012) 64–71.
[52] A.G. Bailey, Colloid thrusters, (1973) 281–283.
[53] S.R. Snarski, P.E. Dunn, Experiments characterizing the interaction between two sprays of electrically charged liquid droplets, 278 (1991) 268–278.
[54] C. Joness, TECHNICAL NOTE MULTIPLE JET ELECTROHYDRODYNAMIC SPRAYING AND APPLICATIONS, 30 (1999) 969–971.
[55] T. Morishita, M. Sugiyama, T. Suzuki, Rotary type electrostatic spray painting device, US Patent 4,369,924. (1983).
[56] E. Law, Electrostatic Atomization and Spraying, in: J.-S. Chang, A. Kelly, J. Crowley (Eds.), Handbook of Electrostatic Processes, Marcel Dekker, Inc., New York, n.d.
[57] A. Jaworek, A.T. Sobczyk, Electrospraying route to nanotechnology: An overview, Journal of Electrostatics. 66 (2008) 197–219.
[58] B. Ksapabutr, M. Panapoy, K. Choncharoen, S. Wongkasemjit, E. Traversa, Investigation of nozzle shape effect on Sm0.1Ce0.9O1.95 thin film prepared by electrostatic spray deposition, Thin Solid Films. 516 (2008) 5618–5624.

[59] C.H. Chen, M.H.J. Emond, E.M. Kelder, B. Meester, J. Schoonman, Electrostatic Sol–Spray Deposition of Nanostructured Ceramic Thin Films, Journal of Aerosol Science. 30 (1999) 959–967.
[60] R. Saf, M. Goriup, T. Steindl, T.E. Hamedinger, D. Sandholzer, G. Hayn, Thin organic films by atmospheric-pressure ion deposition., Nature Materials. 3 (2004) 323–9.
[61] C.H. Chen, A.A.J. Buysman, E.M. Kelder, J. Schoonman, SOLID Fabrication of LiCoO , thin film cathodes for rechargeable lithium battery by electrostatic spray pyrolysis, 80 (1995) 1–4.
[62] A. van Zomeren, E.M. Kelder, J.C.M. Marijnissen, J. Schoonman, The Production of Thin Films of LiMn2O4 by Electrospraying, Journal of Aerosol Science. 25 (1994) 1229–1235.
[63] J. Rutkowskie, Foundations of Balancing at Mobile Phase Interface, Archive Termodynamic. 2 (1981) 75 – 108.
[64] M. Cloupeau, B. Prunet-Foch, Electrohydrodynamic spraying functioning modes: a critical review, Journal of Aerosol Science. 25 (1994).
[65] A. Gañán-Calvo, The surface charge in electrospraying: its nature and its universal scaling laws, Journal of Aerosol Science. 30 (1999) 863–872.
[66] A. Ganan-Calvo, J. Davila, A. Barrero, AND DROPLET SIZE IN THE ELECTROSPRAYING OF LIQUIDS . SCALING LAWS, Journal of Aerosol Science. 28 (1997) 249–275.
[67] J. Fernández de la Mora, The Fluid Dynamics of Taylor Cones, Annual Review of Fluid Mechanics. 39 (2007) 217–243.
[68] R.P. a. Hartman, D.J. Brunner, D.M. a. Camelot, J.C.M. Marijnissen, B. Scarlett, Jet Break-Up in Electrohydrodynamic Atomization in the Cone-Jet Mode, Journal of Aerosol Science. 31 (2000) 65–95.
[69] J. Fernandez De la Mora, I.G. Loscertales, The current emitted by highly conducting Taylor cones, Journal of Fluid Mechanics. 206 (1994) 155 – 184.
[70] J.. López-Herrera, a Barrero, a López, I.. Loscertales, M. Márquez, Coaxial jets generated from electrified Taylor cones. Scaling laws, Journal of Aerosol Science. 34 (2003) 535–552.
[71] R. Bocanegra, D. Galán, M. Márquez, I.G. Loscertales, a. Barrero, Multiple electrosprays emitted from an array of holes, Journal of Aerosol Science. 36 (2005) 1387–1399.
[72] D. Poncelet, V.G. Babak, R.J. Neufeld, M.F. a. Goosen, B. Burgarski, Theory of electrostatic dispersion of polymer solutions in the production of microgel beads containing biocatalyst, Advances in Colloid and Interface Science. 79 (1999) 213–228.
[73] D.P.H. Smith, The Electrohydrodynamic Atomization of Liquids, IEEE Transactions of Industry Applications. I (1986) 527–535.
[74] A. Barrero, I.G. Loscertales, Micro- and Nanoparticles via Capillary Flows, Annual Review of Fluid Mechanics. 39 (2007) 89–106.
[75] C.E. Lapple, Electrostatic Phenomena with Particulates, in: T. Drew (Ed.), Advances in Chemical Engineering, 1st ed., Academic Press, Inc., Menlo Park, CA, 1970.

[76] J.N. Smith, R.C. Flagan, J.L. Beauchamp, Droplet Evaporation and Discharge Dynamics in Electrospray Ionization †, The Journal of Physical Chemistry A. 106 (2002) 9957–9967.
[77] J.-S. Kim, W.-S. Chung, K. Kim, D.Y. Kim, K.-J. Paeng, S.M. Jo, et al., Performance Optimization of Polymer Solar Cells Using Electrostatically Sprayed Photoactive Layers, Advanced Functional Materials. 20 (2010) 3538–3546.
[78] T. Fukuda, K. Takagi, T. Asano, Z. Honda, N. Kamata, K. Ueno, et al., Bulk-heterojunction organic photovoltaic cell fabricated by electrospray deposition method using mixed organic solvent, Physica Status Solidi. (2011) 10–12.
[79] J. Ju, Y. Yamagata, T. Higuchi, Thin-Film Fabrication Method for Organic Light-Emitting Diodes Using Electrospray Deposition, Advanced Materials. 21 (2009) 4343–4347.
[80] K. Choy, W. Bai, S. Charojrochkul, B.C.. Steele, The development of intermediate-temperature solid oxide fuel cells for the next millennium, Journal of Power Sources. 71 (1998) 361–369.
[81] Y. Yu, C.-H. Chen, J.-L. Shui, S. Xie, Nickel-foam-supported reticular CoO-Li2O composite anode materials for lithium ion batteries., Angewandte Chemie (International Ed. in English). 44 (2005) 7085–9.
[82] QCR Solutions, Materials for Organic Solar Cells - PHT105A, (2010).
[83] F. Tran-Van, M. Carrier, C. Chevrot, Sulfonated polythiophene and poly(3,4-ethylenedioxythiophene) derivatives with cations exchange properties, Synthetic Metals. 142 (2004) 251–258.
[84] Q. Qiao, L. Su, J. Beck, J.T. McLeskey, Characteristics of water-soluble polythiophene: TiO2 composite and its application in photovoltaics, Journal of Applied Physics. 98 (2005) 094906.
[85] Y. He, H.-Y. Chen, J. Hou, Y. Li, Indene-C(60) bisadduct: a new acceptor for high-performance polymer solar cells., Journal of the American Chemical Society. 132 (2010) 1377–82.
[86] J.K. Mwaura, M.R. Pinto, D. Witker, N. Ananthakrishnan, K.S. Schanze, J.R. Reynolds, Photovoltaic cells based on sequentially adsorbed multilayers of conjugated poly(p-phenylene ethynylene)s and a water-soluble fullerene derivative., Langmuir : the ACS Journal of Surfaces and Colloids. 21 (2005) 10119–26.
[87] M.A. Faist, T. Kirchartz, W. Gong, R.S. Ashraf, I. McCulloch, J.C. de Mello, et al., Competition between the charge transfer state and the singlet states of donor or acceptor limiting the efficiency in polymer:fullerene solar cells., Journal of the American Chemical Society. 134 (2012) 685–92.
[88] C. Richardson, D. Schuster, S. Wilson, Synthesis and characterization of water-soluble amino fullerene derivatives, Organic Letters. 2 (2000) 1011–4.
[89] Sigma Aldrich, C60 Pyrridoline tris-acid - 709085, (2012).
[90] R. Hengerer, B. Bolliger, M. Erbudak, M. Grätzel, Structure and stability of the anatase TiO 2(101) and (001) surfaces, Surface Science. 460 (2000) 162–169.
[91] J. Salafsky, Exciton dissociation, charge transport, and recombination in ultrathin, conjugated polymer-TiO_ {2} nanocrystal intermixed composites, Physical Review B. 59 (1999) 885–894.

[92] Q. Qiao, Green Organic Solar Cells from a Water Soluble Polymer and Nanocrystalline TiO2, Virginia Commonwealth University, 2006.
[93] R. Kniprath, J.T. McLeskey, J.P. Rabe, S. Kirstein, Nanostructured solid-state hybrid photovoltaic cells fabricated by electrostatic layer-by-layer deposition, Journal of Applied Physics. 105 (2009) 124313.
[94] Q. Qiao, J. Beck, R. Lumpkin, J. Pretko, J.T. McLeskey Jr., A comparison of fluorine tin oxide and indium tin oxide as the transparent electrode for P3OT/TiO2 solar cells, Solar Energy Materials and Solar Cells. 90 (2006) 1034–1040.
[95] J. Yang, A. Garcia, T.-Q. Nguyen, Organic solar cells from water-soluble poly(thiophene)/fullerene heterojunction, Applied Physics Letters. 90 (2007) 103514.
[96] S.A. McClure, B.J. Worfolk, D.A. Rider, R.T. Tucker, J.A.M. Fordyce, M.D. Fleischauer, et al., Electrostatic layer-by-layer assembly of CdSe nanorod/polymer nanocomposite thin films., ACS Applied Materials & Interfaces. 2 (2010) 219–29.
[97] A.J. Miller, R.A. Hatton, S.R.P. Silva, Water-soluble multiwall-carbon-nanotube-polythiophene composite for bilayer photovoltaics, Applied Physics Letters. 89 (2006) 123115.
[98] J.H. Cho, J. Lee, Y. Xia, B. Kim, Y. He, M.J. Renn, et al., Printable ion-gel gate dielectrics for low-voltage polymer thin-film transistors on plastic., Nature Materials. 7 (2008) 900–6.
[99] A. Babel, J.D. Wind, S.A. Jenekhe, Ambipolar Charge Transport in Air-Stable Polymer Blend Thin-Film Transistors, Advanced Functional Materials. 14 (2004) 891–898.
[100] J.W. Baur, S. Kim, P.B. Balanda, J.R. Reynolds, M.F. Rubner, Thin-Film Light-Emitting Devices Based on Sequentially Adsorbed Multilayers of Water-Soluble Poly(p-phenylene)s, Advanced Materials. 10 (1998) 1452–1455.
[101] H. Zhang, Z. Cui, Y. Wang, K. Zhang, X. Ji, C. Lü, et al., From Water-Soluble CdTe Nanocrystals to Fluorescent Nanocrystal–Polymer Transparent Composites Using Polymerizable Surfactants, Advanced Materials. 15 (2003) 777–780.
[102] C. Chen, E. Kelder, P. van der Put, J. Schoonman, Morphology control of thin LiCoO2 films fabricated using the electrostatic spray deposition (ESD) technique, Journal of Materials Chemistry. 6 (1996) 765–771.
[103] B.-H. Hwang, C.-L. Chang, C.-S. Hsu, C.-Y. Fu, Electrostatic spray deposition of NiO/CGO films, Journal of Physics D: Applied Physics. 40 (2007) 3448–3455.
[104] R. Neagu, D. Perednis, A. Princivalle, E. Djurado, Initial Stages in Zirconia Coatings Using ESD, Chemistry of Materials. 17 (2005) 902–910.
[105] J. Elson, Theory of light scattering from a rough surface with an inhomogeneous dielectric permittivity, Physical Review B. 30 (1984).
[106] D. Aspnes, Optical properties of thin films, Thin Solid Films. 89 (1982) 249–262.
[107] H. Hoppe, N.S. Sariciftci, Morphology of polymer/fullerene bulk heterojunction solar cells, Journal of Materials Chemistry. 16 (2006) 45.
[108] D. Gebeyehu, C. Brabec, Hybrid solar cells based on dye-sensitized nanoporous TiO2 electrodes and conjugated polymers as hole transport materials, Synthetic Metals. 125 (2001) 279–287.
[109] W.U. Huynh, J.J. Dittmer, A.P. Alivisatos, Hybrid nanorod-polymer solar cells., Science (New York, N.Y.). 295 (2002) 2425–7.

[110] E. Hendry, F. Wang, J. Shan, T. Heinz, M. Bonn, Electron transport in TiO2 probed by THz time-domain spectroscopy, Physical Review B. 69 (2004) 081101.
[111] R. Könenkamp, Carrier transport in nanoporous TiO2 films, Physical Review B. 61 (2000) 57–64.
[112] K.M. Coakley, B.S. Srinivasan, J.M. Ziebarth, C. Goh, Y. Liu, M.D. McGehee, Enhanced Hole Mobility in Regioregular Polythiophene Infiltrated in Straight Nanopores, Advanced Functional Materials. 15 (2005) 1927–1932.
[113] A.J. Mozer, N.S. Sariciftci, Negative electric field dependence of charge carrier drift mobility in conjugated, semiconducting polymers, Chemical Physics Letters. 389 (2004) 438–442.
[114] A. Mozer, N. Sariciftci, A. Pivrikas, R. Österbacka, G. Juška, L. Brassat, et al., Charge carrier mobility in regioregular poly(3-hexylthiophene) probed by transient conductivity techniques: A comparative study, Physical Review B. 71 (2005) 035214.
[115] H. Sirringhaus, N. Tessler, R. Friend, Integrated optoelectronic devices based on conjugated polymers, Science (New York, N.Y.). 280 (1998) 1741–4.
[116] X. Yang, J. Loos, S.C. Veenstra, W.J.H. Verhees, M.M. Wienk, J.M. Kroon, et al., Nanoscale morphology of high-performance polymer solar cells., Nano Letters. 5 (2005) 579–83.
[117] J. Nunzi, Organic photovoltaic materials and devices, Comptes Rendus Physique. 3 (2002) 523–542.
[118] A. Breeze, Z. Schlesinger, S. Carter, P. Brock, Charge transport in TiO2/MEH-PPV polymer photovoltaics, Physical Review B. 64 (2001) 1–9.
[119] T.-W. Zeng, H.-H. Lo, C.-H. Chang, Y.-Y. Lin, C.-W. Chen, W.-F. Su, Hybrid poly (3-hexylthiophene)/titanium dioxide nanorods material for solar cell applications, Solar Energy Materials and Solar Cells. 93 (2009) 952–957.
[120] P. Ravirajan, S. a. Haque, J.R. Durrant, D.D.C. Bradley, J. Nelson, The Effect of Polymer Optoelectronic Properties on the Performance of Multilayer Hybrid Polymer/TiO2 Solar Cells, Advanced Functional Materials. 15 (2005) 609–618.
[121] D. Gebeyehu, C.J. Brabec, N.S. Sariciftci, D. Vangeneugden, R. Kiebooms, Hybrid solar cells based on dye-sensitized nanoporous TiO2 electrodes and conjugated polymers as hole transport materials, 125 (2002) 279–287.
[122] A. Andersson, N. Johansson, P. Bröms, N. Yu, D. Lupo, W.R. Salaneck, Fluorine Tin Oxide as an Alternative to Indium Tin Oxide in Polymer LEDs, Advanced Materials. 10 (1998) 859–863.
[123] P. Anderson, Work Function of Gold, Physical Review. 115 (1959) 553–554.
[124] S. Aazou, E.M. Assaid, E. Jadida, MODELLING REAL PHOTOVOLTAIC SOLAR CELL USING MAPLE, (2009) 394–397.
[125] A. Jain, A. Kapoor, Exact analytical solutions of the parameters of real solar cells using Lambert W-function, Solar Energy Materials and Solar Cells. 81 (2004) 269–277.
[126] L. Schmidt-Mende, M. Grätzel, TiO2 pore-filling and its effect on the efficiency of solid-state dye-sensitized solar cells, Thin Solid Films. 500 (2006) 296–301.
[127] H. Han, U. Bach, Y.-B. Cheng, R. a. Caruso, Increased nanopore filling: Effect on monolithic all-solid-state dye-sensitized solar cells, Applied Physics Letters. 90 (2007) 213510.

[128] P. Ravirajan, S. a. Haque, J.R. Durrant, D.D.C. Bradley, J. Nelson, The Effect of Polymer Optoelectronic Properties on the Performance of Multilayer Hybrid Polymer/TiO2 Solar Cells, Advanced Functional Materials. 15 (2005) 609–618.
[129] A.F. Nogueira, C. Longo, M.A. De Paoli, Polymers in dye sensitized solar cells: overview and perspectives, Coordination Chemistry Reviews. 248 (2004) 1455–1468.
[130] Y. Shen, K. Li, N. Majumdar, J.C. Campbell, M.C. Gupta, Bulk and contact resistance in P3HT:PCBM heterojunction solar cells, Solar Energy Materials and Solar Cells. 95 (2011) 2314–2317.
[131] P. Schilinsky, C. Walfauf, J. Hauch, C.J. Brabec, Simulation of light intensity dependent current characteristics of polymer solar cells, Journal of Applied Physics. 95 (2004) 2816.
[132] G. del Pozo, B. Romero, B. Arredondo, Evolution with annealing of solar cell parameters modeling the S-shape of the current–voltage characteristic, Solar Energy Materials and Solar Cells. 104 (2012) 81–86.
[133] S. Tanaka, Performance simulation for dye-sensitized solar cells: Toward high efficiency and solid state, Japanese Journal of Applied Physics. 40 (2001) 97–107.
[134] J. Song, Z. Xu, F. Zhang, S. Zhao, T. Hu, J. Li, et al., The effect of annealing treatment on the performance of bulk heterojunction solar cells with donor and acceptor different weight ratios, Science in China Series G: Physics, Mechanics and Astronomy. 52 (2009) 1606–1610.
[135] Y. Zhang, Z. Li, S. Wakim, S. Alem, S.-W. Tsang, J. Lu, et al., Bulk heterojunction solar cells based on a new low-band-gap polymer: Morphology and performance, Organic Electronics. 12 (2011) 1211–1215.
[136] A. Elschner, S. Kirchmeyer, W. Lovenich, U. Merker, K. Reuter, The complete chapter on PEDOT:PSS, in: PEDOT - Principles and Applications of an Intrinsically Conductive Polymer, CRC Press, 2011: pp. 113–165.
[137] M. Campoy-Quiles, T. Ferenczi, T. Agostinelli, P.G. Etchegoin, Y. Kim, T.D. Anthopoulos, et al., Morphology evolution via self-organization and lateral and vertical diffusion in polymer:fullerene solar cell blends., Nature Materials. 7 (2008) 158–64.
[138] Z. Xu, L.-M. Chen, G. Yang, C.-H. Huang, J. Hou, Y. Wu, et al., Vertical Phase Separation in Poly(3-hexylthiophene): Fullerene Derivative Blends and its Advantage for Inverted Structure Solar Cells, Advanced Functional Materials. 19 (2009) 1227–1234.
[139] S.-E. Park, J.-Y. Hwang, K. Kim, B. Jung, W. Kim, J. Hwang, Spray deposition of electrohydrodynamically atomized polymer mixture for active layer fabrication in organic photovoltaics, Solar Energy Materials and Solar Cells. 95 (2011) 352–356.
[140] J.T. McLeskey Jr., Q. Qiao, Nanostructured organic solar cells, in: 2011: pp. 147–186.